coatings

MDPI

Article

Electroless Deposits of ZnO and Hybrid ZnO/Ag Nanoparticles on Mg-Ca0.3 Alloy Surface: Multiscale Characterization

José Luis González-Murguía [1], Veleva Lucien [1,*] and Mario Alpuche-Avilés [2]

[1] Applied Physics Department, Center for Investigation and Advanced Study (CINVESTAV), Mérida 97310, Mexico; josel.gonzalez@cinvestav.mx
[2] Department of Chemistry, University of Nevada, Reno, NV 89557, USA; malpuche@unr.edu
* Correspondence: veleva@cinvestav.mx; Tel.: +52-999-942-9447

Abstract: ZnO and hybrid of ZnO/Ag structures in the nanometer size were electroless deposited on the Mg-Ca0.3 alloy surface, achieved from aqueous solutions (10^{-3} M at 21 °C) of ZnO (suspension), $Zn(NO_3)_2$ and $AgNO_3$. The surface characterization of the deposits was carried out by Scanning Electron Microscopy-Energy Dispersive Spectroscopy (SEM-EDS), X-Ray Photoelectron Spectroscopy (XPS), Fourier transform infrared (FTIR), UV-Visible and Raman spectroscopy. The nanoparticles (NPs) area size distribution analysis revealed that the average of ZnO-NPs was ~85 nm. Likewise, the Ag-NPs of electroless deposits had an average area size of ~100 nm and nucleated in the vicinity of ZnO-NPs as Ag^+ ions have been attracted by the negatively charged O^{2-} atoms of the Zn-O dipole. The ZnO-NPs had the wurtzite structure, as indicated by Raman spectroscopy analysis and XRD complementary analysis. The UV-Visible spectroscopy analysis gave a peak at ~320 nm associated with the decrease in the imaginary part (k) of the refractive index of Ag-NPs. On the Mg-Ca0.3 surface, MgO, $Mg(OH)_2$ and $MgCO_3$ are present due to the Mg-matrix. XRD spectra of Ag-NPs indicated the presence of planes arranged with the FCC hexagonal structure. The reported hybrid ZnO/Ag electroless deposits of NPs are of interest for temporary implant devices, providing antibacterial properties to Mg-Ca0.3 surface, a widely used biodegradable material.

Keywords: Mg-Ca alloy; electroless deposits; ZnO; Ag; nanoparticles; XPS; SEM-EDS; UV-Vis; Raman

Citation: González-Murguía, J.L.; Lucien, V.; Alpuche-Avilés, M. Electroless Deposits of ZnO and Hybrid ZnO/Ag Nanoparticles on Mg-Ca0.3 Alloy Surface: Multiscale Characterization. *Coatings* **2022**, *12*, 1109. https://doi.org/10.3390/coatings12081109

Academic Editor: Marcin Pisarek

Received: 7 July 2022
Accepted: 29 July 2022
Published: 3 August 2022

1. Introduction

Magnesium and its alloys have attracted research interest as biodegradable and biocompatible materials when used as temporary implants in physiological media, presenting an alternative over the non-resorbable biomaterials [1–10]. During the biodegradation process, magnesium Mg^{2+} ions are released, which are non-toxic, and used for the synthesis of proteins, activating a variety of enzymes and regulating the central nervous and neuromuscular systems; these ions also help regulate blood glucose, blood pressure, and play an important role in the prevention and treatment of diabetes and cardiovascular diseases [11–18]. Because of these many advantages, Mg and its alloys are potential materials for the design of new temporary orthopedic devices, providing mechanical properties similar to those of the human bone, maintaining mechanical integrity on a scale of 12–18 weeks, while the bone tissue heals [5,19–21]. However, to help fight against bacterial infection during and after surgery requires an additional modification of the material surface to achieve antibacterial activity [19,22–28]. According to a prior report, the hybrid structures are based on the combination of deposited semiconductor oxides (micro- or nanostructured) and noble metal nanoparticles (NPs) on the implantable metallic surfaces is a current and pressing research topic in this area to improve antibacterial properties to these alloys [12,13,24,28–34].

In this aspect, ZnO, a wide-bandgap semiconductor oxide and its nanoparticles (NPs), known for their mechanical resistance [33], have been considered one of the novel antibacterial biologically active materials through several possible mechanisms. On the one hand,

the release of Zn^{2+} ions in physiological media results in the activation of antibacterial mechanisms against different bacteria species [34]. The antibacterial activity of ZnO-NPs has been suggested to be based on their ability to induce excessive generation (stress) of Reactive Oxygen Species (ROS), such as superoxide anion (O^{2-}), hydroxyl radicals (OH^{-}) and the production of hydrogen peroxide (H_2O_2). This oxidative stress results in the formation of electron losses that cause cell death in different bacteria [29]. One study reports that the possible antibacterial mechanism of ZnO-NPs against the bacteria *Escherichia coli* is due to the NPs coming into direct contact with the phospholipid bilayer of the bacteria membrane, destroying its integrity and causing cell death [32].

Several studies report the antibacterial efficiency of Ag-NPs against different bacteria (*Straphylococcus Epidermis*, *Straphylococcus Aureus*, *Pseudomonas Aeruginosa*, *Escherichia Coli*, *Klepsiella Pneumonia*, *Citrobacter Koseri* and *Salmonella Typhii*), although the mechanism of action is not yet fully understood [27,29,30,35]. However, it has been shown that Ag-NPs, by binding to and infiltrating the cell wall, may cause physical changes and damage to the cell wall, leading to leakage of cell content and subsequent destruction of the bacteria [36,37]. Some reported results have demonstrated that the antibacterial activity of Ag-NPs against *Escherichia coli* has been associated with the perforation of its cell wall, where an accumulation of Ag^{+} occurs, resulting in cell death [29].

In this work, we report the deposition of ZnO and Ag because semiconductor oxides, such as ZnO, may provide a large surface area that serves as better structural support for the deposits of noble metals such as Ag-NPs. In this regard, the Ag-NPs deposit on the ZnO surface may considerably increase the antibacterial activity against Gram-positive and Gram-negative strains [12,13,38–40]. For example, one study reported that composite coatings of Zn and Ag particles (Zn/Ag), electrodeposited on AISI 1019 steel, may improve the antibacterial properties of the steel surface [41]. A separate study found that an Ag-ZnO nanostructured coating on Mg-2Ca-0.5Mn-6Zn was prepared through physical vapor deposition (PVD), and it was found that the corrosion resistance and antibacterial activity of the coated surface were improved in Simulated Body Fluid (SBF) physiological media, suggesting that this coating is suitable for permanent implant applications [42]. Another report of a composite coating of ZnO deemed nanostructured ZnO/$Ca_3ZrSi_2O_9$ was fabricated as an over-layer on Mg-Zn-Ca surface via physical vapor deposition (PVD) coupled with electrophoretic deposition (EPD), and it was considered as another suitable coating for Mg alloy; in this material intended for a permanent orthopedic implant, the authors reported improved corrosion resistance in SBF media with better antibacterial activity [43]. Here, we present the simple electroless deposition of ZnO and ZnO/Ag coatings on Mg-Ca0.3 alloy, which does not require vapor phase deposition, complex agents or reductive additives for the preparation of the solutions. We demonstrate that ZnO/Ag hybrid coating is of interest for temporary implant materials, and because of the intrinsic provisional applications of the materials, the coating should provide antibacterial properties but without increasing the corrosion resistance, as in the examples above [41–43].

Mg-Ca alloys have attracted significant attention in material bioengineering in the design of orthopedic implants and bone tissue because the Ca element has a high natural abundance in the human body, mainly in bones and teeth [44]. The Ca^{2+} ion and its compounds (phosphate type) can be tolerated (low toxicity) by the human body at relatively high levels of ~4 g/day. The Mg-Ca alloys are also mechanically compatible with bone, biodegradable and exhibit interesting characteristics as a potential material for implants, providing cell adhesion (osteoconductivity) and cell growth stimulation on the implant surface [44,45]. In a previous study, we reported the antibacterial effect of Ag-NPs electroless deposited on the Mg-Ca0.3 surfaces, with a percentage inhibition of diameter growth (PIDG) of up to 64% against *E. coli* and 83% against *S. aureus* [45].

Among the methods developed for the deposition of the coating on metals surface, the electroless deposition (ELD) method without external polarization is well-known [46–49]. Electroless deposition is usually limited to a few monolayers without the addition of a catalyst [50]. The objective of this work is to obtain and provide a multiscale characterization

of ZnO-NPs and hybrid ZnO/Ag -NPs electroless deposited on the surface of the Mg-Ca0.3 alloy, obtained from aqueous solutions (10^{-3} M, at 21 °C) of ZnO, $Zn(NO_3)_2$ and $AgNO_3$. The characterization of the nanoparticles was carried out by SEM-EDS, XPS, FTIR, UV-Visible and Raman spectroscopy techniques. The Ag-NPs size and surface distribution were also determined.

2. Materials and Methods

2.1. Samples and Solution Preparation

The Mg-Ca0.3 alloy (0.3 wt.%) was supplied by Helmholtz-Zentrum Hereon, Institute for Material and Process Design (Geesthacht, Germany); the alloy was manufactured by extrusion in the form of 1 cm diameter cylindrical bars. Table 1 presents the nominal composition (wt.%) according to the manufacturer. The Mg-Ca0.3 samples (0.78 cm^2) were sanded with 600 to 4000 grit SiC paper with ethanol as a lubricant, then sonicated for 5 min and dried at room temperature.

Table 1. Nominal composition of the extruded Mg-Ca0.3 alloy.

Element	Mg	Ca	Al	Zn	Fe	Cu	Ni
Composition (wt.%)	Bal.	0.23	0.016	0.006	0.0019	0.0019	0.0014

Electroless deposits of ZnO and ZnO/Ag on Mg-Ca0.3 surface (0.78 cm^2) were achieved by immersion in 10^{-3} M aqueous suspensions of ZnO and solutions of $Zn(NO_3)_2$ (for 5 min) and $AgNO_3$ (for 3 min) at 21 °C [51–55]. Consequently, the previously ZnO coated samples were immersed in 10^{-3} M $AgNO_3$ solution [56–68] for 3 min (Table 2). The aqueous solutions were prepared from analytical grade reagents (Sigma-Aldrich, St. Louis, MO, USA) and deionized ultrapure water (18.2 MΩ cm). The measured pH (pH60, Apera Instruments, Columbus, OH, USA) and ion content of the solutions (photometry HI83200, Hanna Instruments, Woonsocket, RI, USA) are presented in Table 2. Note that the ion concentrations were measured using a standard method and reactants (Hanna Instruments), and we report their average and standard deviation after three replicates.

Table 2. pH and Zn^{2+} and Ag^{+} ion ions concentrations of the aqueous solutions and their pH, used for electroless deposition.

Solution (10^{-3} M)	Concentration (mg L^{-1})	Zn^{2+} Ions (mg L^{-1})	Ag^{+} Ions (mg L^{-1})	pH
ZnO	83.38	1.05 ± 0.32	—	7.11 ± 0.05
$Zn(NO_3)_2$	297.48	66.7 ± 1.21	—	6.45 ± 0.03
$AgNO_3$	169.87	—	108.8 ± 1.72	6.22 ± 0.02

Note: The $Zn(NO_3)_2$ aqueous solution contains higher Zn^{2+} ion concentration.

The coated samples were taken to the oven (Thermolyne 46100 High Temperature Chamber Furnace, Dubuque, IA, USA) and baked at 200 °C for 48 h so that at this temperature, strapped water would be removed from their structure [55,59–61].

2.2. Electroless Deposits of ZnO-NPs and Hybrid ZnO/Ag-NPs on Mg-Ca0.3 Surface and Their Characterization

The morphology and composition of the deposits on the Mg-Ca0.3 surfaces were characterized by: SEM-EDS (SEM-EDS, XL-30 ESEM-JEOL JSM-7600F, JEOL Ltd., Tokyo, Japan) and XPS (K-Alpha Surface Analyzer, ThermoFisher Scientific, Waltham, MA, USA). The binding energies of all XPS spectra were corrected so that the C1s peak would be at 284.8 eV. The ZnO and ZnO/Ag deposits were characterized by the UV-Vis technique (AVASpec 2048, AVANTES, Eerbeek, The Netherlands), FTIR (Specular Apertured Grazing Angle, SAGA; Nicolet nexus 670, ThermoFisher Scientific, Waltham, MA, USA), XRD (Siemens D-5000 diffractometer, Grazing Beam 1 Th, 34 kV 25 mA, Munich, Germany) and

Raman spectroscopy (Ar-ion laser of 488 nm, 50× of 1800 grooves/mm, spectral resolution of 1 cm^{-1}; confocal Raman alpha300 WITec GmbH, Ulm, Germany).

3. Results and Discussion

3.1. Surface Characterization of Mg-Ca0.3

3.1.1. SEM-EDS Analysis

Figure 1 presents the SEM image (2000×) of the freshly polished reference surface of Mg-Ca0.3. The EDS analysis of the zones (labeled as 1 and 2, Figure 1b) revealed the highest value for the element Mg (the metallic matrix), as well as suggested the presence of MgO and Mg_2Ca particles, widely reported in the metallurgy literature [59–62].

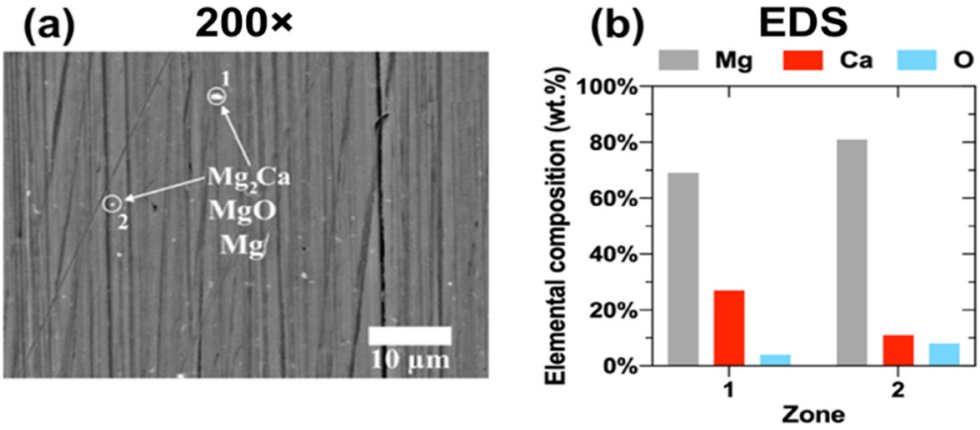

Figure 1. (**a**) SEM image (2000×) of Mg-Ca0.3 reference sample and (**b**) EDS analysis of sites labeled on the SEM image and the suggested compounds.

Figure 2 compares the SEM images (200× and 5000×) of the Mg-Ca0.3 surfaces on which ZnO was electroless deposited from the 10^{-3} M solutions of ZnO (Figure 2a,b) and $Zn(NO_3)_2$ (Figure 2d,e).

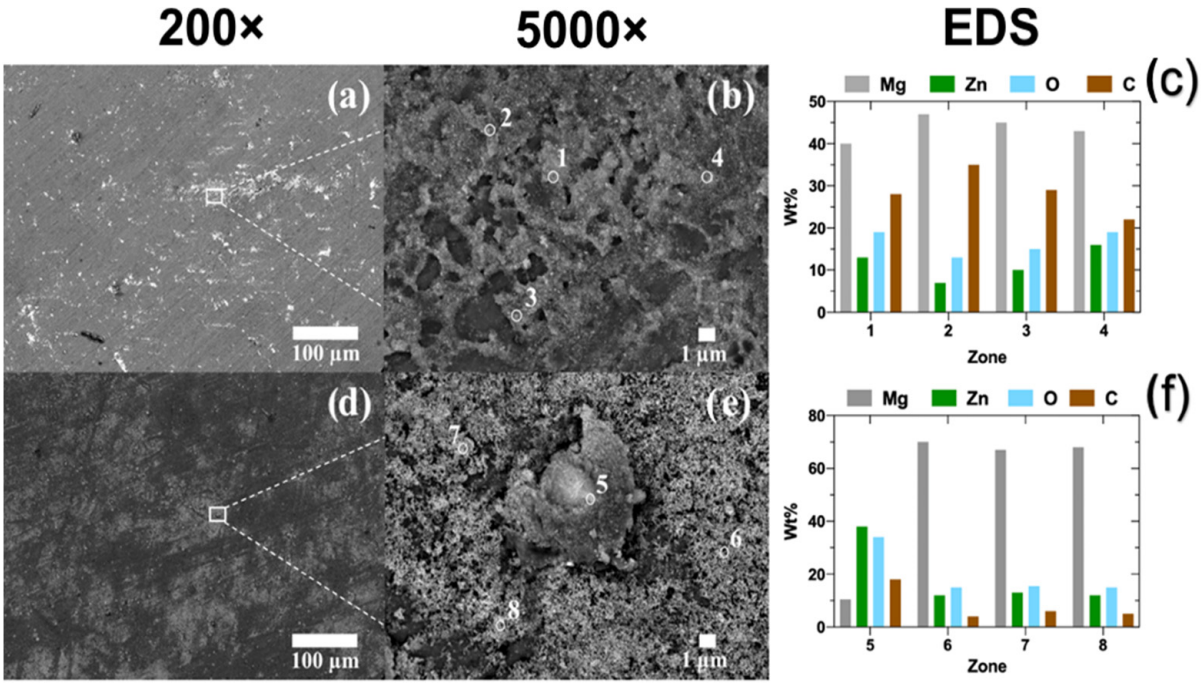

Figure 2. SEM images (200× and 5000×) and EDS analysis of ZnO electroless deposits on the Mg-Ca0.3 surfaces, obtained from two 10^{-3} M aqueous solutions (at 21 °C): (**a**–**c**) ZnO and (**d**–**f**) $Zn(NO_3)_2$.

The deposits showed the tendency of a cluster formation, more nucleated on the substrate surface (Figure 2d,e) when achieved from the $Zn(NO_3)_2$ solution (Table 2). The EDS analysis (wt.%) of the zones labeled as 1–8 (Figure 2b,c,e,f) indicated that besides the main component of Mg (the matrix of the alloy), Zn and O are present, and C at relatively lower content.

3.1.2. XPS Analysis

In order to correlate the EDS elemental quantification analysis (Figure 2) with the composition of electroless deposits formed on the Mg-Ca0.3 surface, XPS analysis was carried out; Figure 3 presents the high-resolution spectra of Mg, Zn, O and C elements. The O1s spectrum shows a maximum peak at ≈531.9 eV associated with the presence of hydroxide [66–70], as also two deconvoluted peaks at ≈531.2 eV ascribed to metal oxide [71–77] and at ≈532.3 eV belonged to inorganic carbonate [66,67,73,78–80]. The high-resolution spectrum of Mg2p presented a maximum peak at ≈50.2 eV associated with the presence of MgO [67,69,71,72,81]; likewise, two deconvoluted peaks were detected at ≈49.8 eV ascribed to $Mg(OH)_2$ [66–69], and at ≈51.2 eV suggesting the presence of $MgCO_3$ [66,67,73]. The high-resolution spectrum of C1s presented a maximum peak at ≈287.9 eV associated with the presence of carbon in $MgCO_3$ [66,67,73]. Because of the spin-orbit splitting, the Zn2p spectrum has two peaks: at ≈1045.7 eV, characteristic of ZnO [66,67,73–75,78–81], and at ≈1022.5 eV associated with the presence of $ZnCO_3$. According to a previous study, MgO has shown a high potential for CO_2 adsorption due to its high porosity and the tunable nature of the pores [82]. The formation of $ZnCO_3$ is associated with the CO_2 adsorption on polar surfaces of ZnO, where CO_2 dissociates at oxygen vacancy [83]. It may be noted that the deposits obtained from $Zn(NO_3)_2$ solution exhibited ≈3 times higher intensity of the Zn2p spectrum peaks (Figure 3b) than those of the deposits achieved from the ZnO solution (Figure 3a). These facts correlate with the EDS analysis (Figure 2).

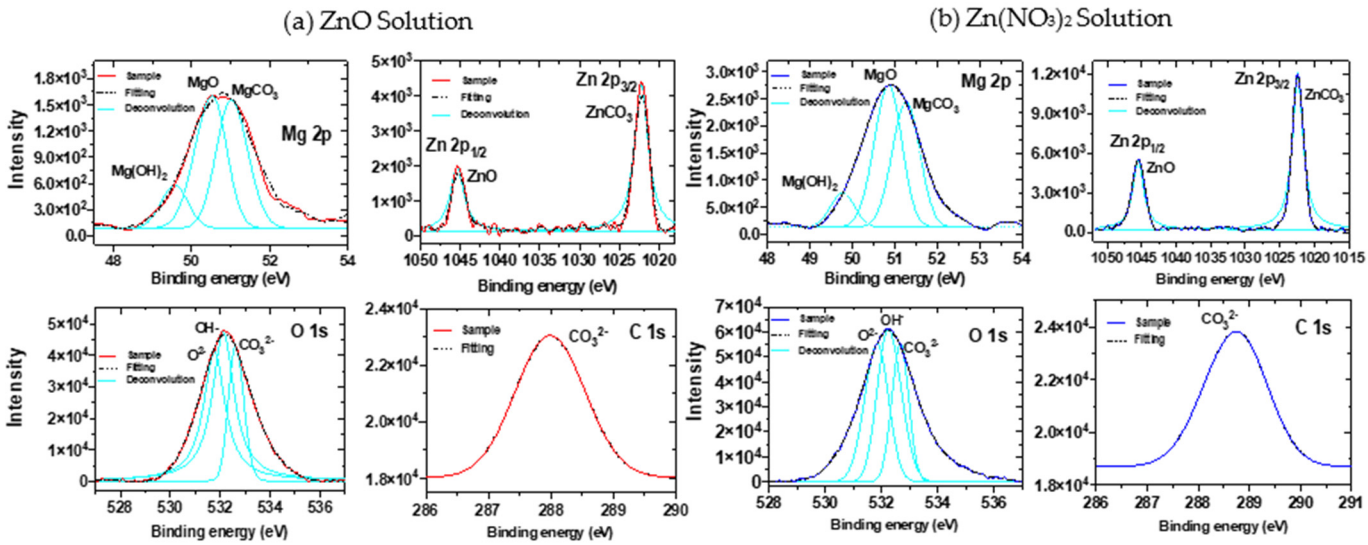

Figure 3. XPS spectra of ZnO electroless deposits on Mg-Ca0.3, obtained from 10^{-3} M aqueous solutions (at 21 °C): (**a**) ZnO and (**b**) $Zn(NO_3)_2$.

3.1.3. EDS Mapping of the Elements

Figure 4 presents the EDS maps (200×) of Mg, Zn, O and C elements (wt.%) and their distribution as a part of the ZnO electroless deposits on Mg-Ca0.3 (Figure 4a,b). As it was suggested by the XPS analysis (Figure 3), the Mg, O, C and Zn belong to the MgO, $Mg(OH)_2$, $MgCO_3$, $ZnCO_3$ and ZnO compounds. The deposits obtained from $Zn(NO_3)_2$ aqueous

solution (Table 2) presented ≈2 times higher concentration of Zn (Figure 4b) compared to the content of Zn of the deposit from ZnO solution (Figure 4a).

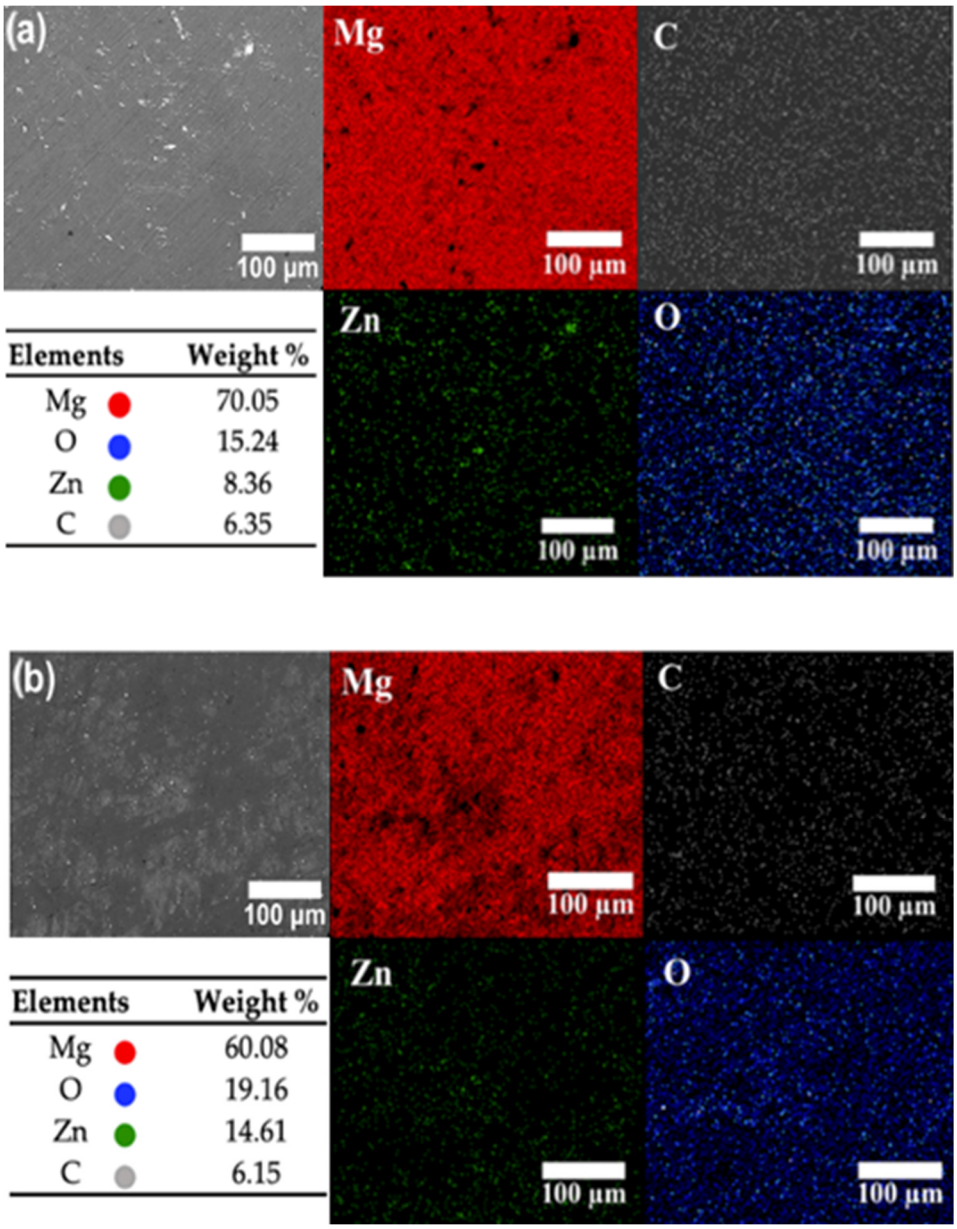

Figure 4. EDS mapping (200×) of the elements present in the electroless deposits on Mg-Ca0.3, obtained from 10^{-3} M solutions of ZnO (**a**) and $Zn(NO_3)_2$ (**b**).

3.1.4. ZnO Nanoparticle Size Distribution

Figure 5 displays the particle size distribution of ZnO (this analysis was carried out with the ImageJ software of the National Institutes of Health, Bethesda, Maryland, USA). Note that the average size of an individual particle is ≈90 ± 3 nm (Figure 5a) and ≈79 ± 3 nm (Figure 5b). Furthermore, the frequency of these ZnO nanoparticles is ≈2 times higher for the ZnO deposits (Figure 5b) obtained from the $Zn(NO_3)_2$ solution (Table 2) and apparently more dispersed on the surfaces (Figure 2). Figure 5a′,b′ present the SEM images (100,000×) of isolated particles on the Mg-Ca0.3 surface for both deposits, which size agrees with the particle distribution analysis (88.3, 92.5 and 81.6 nm).

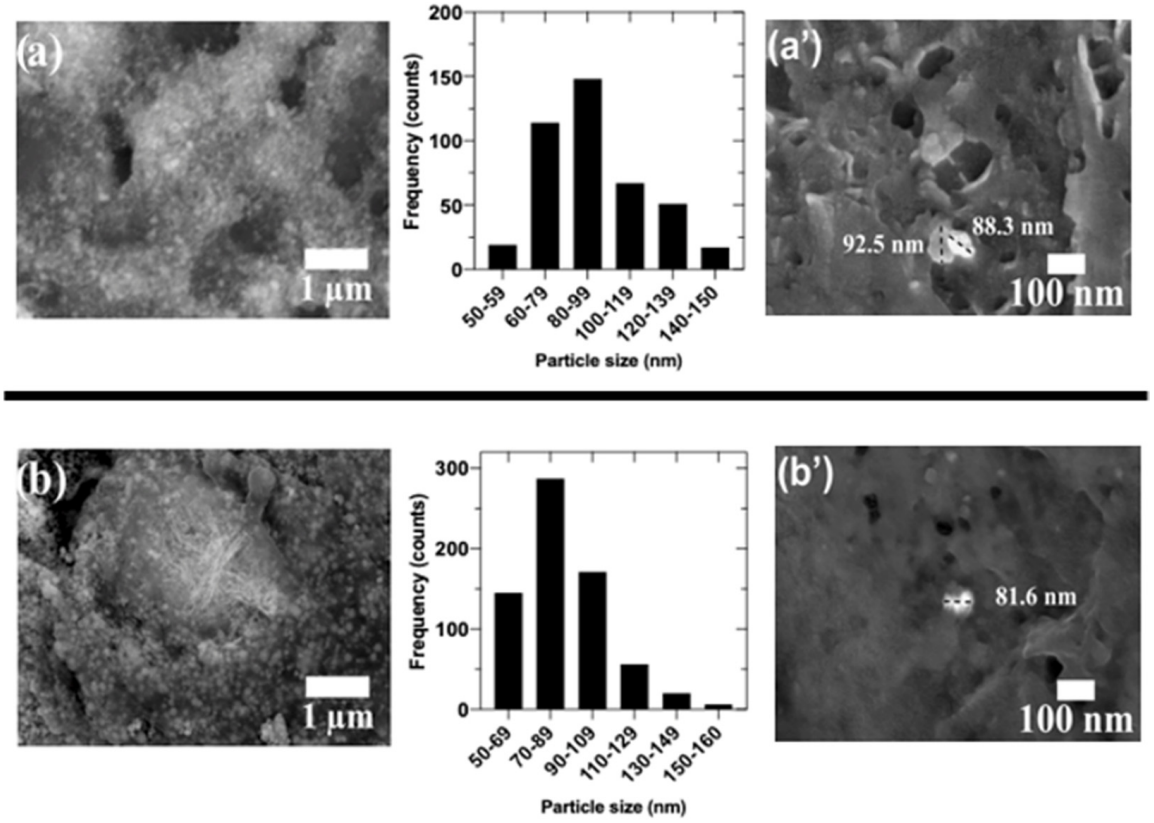

Figure 5. SEM images (20,000×), particle size distribution and isolated particle images (100,000×) of electroless deposits on Mg-Ca0.3 obtained from: (**a**,**a'**) 10^{-3} M ZnO and (**b**,**b'**) 10^{-3} M $Zn(NO_3)_2$ solutions.

3.1.5. FTIR Analysis

Figure 6 shows the FTIR spectra (Specular Apertured Grazing Angle) of the ZnO electroless deposits on the Mg-Ca0.3 surfaces. The peak at ≈650 cm^{-1} is characteristic of the Mg-O vibration [84,85], while the narrow peaks at ≈3680 cm^{-1} and ≈1510 cm^{-1} were attributed to the vibration of the structural hydroxyl group in $Mg(OH)_2$ [85,86], both compounds as corrosion products formed in aqueous solutions (Figure 6b,c). Additionally, very faint bands between ≈960 and 1140 cm^{-1} are assigned to a very small amount of poorly crystalline $ZnCO_3$ (smithsonite) [87,88]. The peak observed at ≈1430 cm^{-1} was associated with $MgCO_3$ [87,89] and those at ≈860 cm^{-1} and ≈600 cm^{-1} as characteristic of the Zn-O bond [90–95].

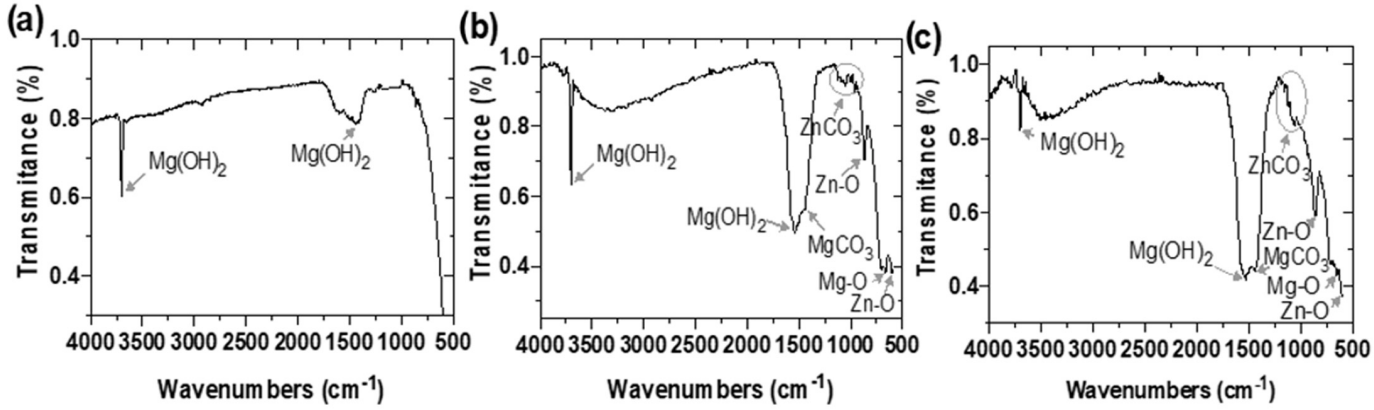

Figure 6. FTIR spectra of (**a**) Mg-Ca0.3 surface and electroless ZnO deposits, obtained from aqueous solutions (10^{-3} M, at 21 °C) of (**b**) ZnO and (**c**) $Zn(NO_3)_2$.

3.1.6. UV-Vis Spectroscopy Analysis

This analysis was carried out to characterize the electroless ZnO deposits on Mg-Ca0.3 surface. The UV-Vis spectra (Figure 7) confirmed the presence of the characteristic absorption peak at ≈380 nm, which is consistent with the intrinsic band-gap of ZnO due to the electronic transition from the valence band to the conduction band (O2p to Zn3d) [96,97]. Such peak was reported for ZnO obtained by the sol-gel method [98] and from colloidal solutions [99,100], as well as by spontaneous hydrolysis [101] and alkaline hydrolysis [102].

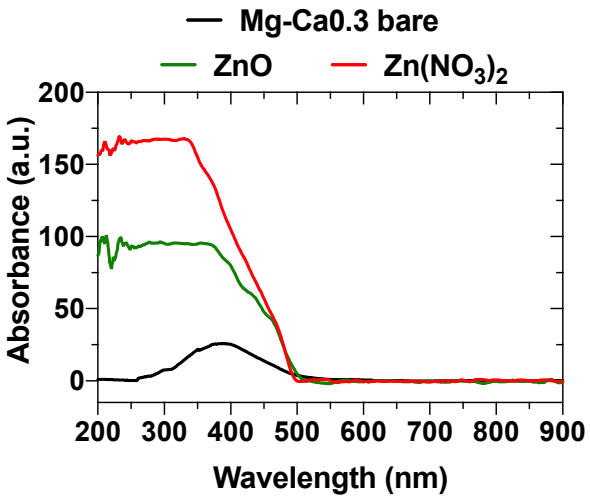

Figure 7. UV-Vis spectra of Mg-Ca0.3 surface and electroless ZnO deposits, obtained from aqueous suspension solutions (10^{-3} M, at 21 °C) and solutions of ZnO and $Zn(NO_3)_2$.

3.1.7. Raman Spectroscopy Analysis

Raman spectroscopy study was carried out on the ZnO deposits (Figure 8) as a sensitive diagnostic tool for the nanocrystal structure and morphology. It is known that ZnO is a semiconductor (a direct wide band gap of 3.37 eV and a large excitation binding energy of 60 meV), and the ZnO surface can be described as a dipole oriented (+ −), negatively charged by the O^{2-} and positively charged by the Zn^{2+} ions, tetrahedrally coordinated and resulting in spontaneous polarization. The hexagonal ZnO wurtzite structure belongs to the C^4_{6v} group. According to this group theory, A1 + 2E2 + E1 are Raman-active modes, corresponding to optical phonons of Low and High frequency.

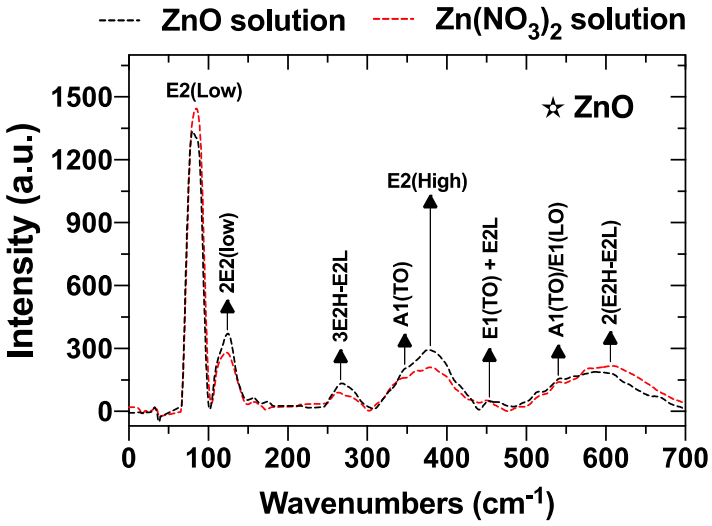

Figure 8. Raman spectra of electroless ZnO deposits on Mg-Ca0.3 surfaces, obtained as in Figure 7.

The Raman-scattering spectra of ZnO electroless deposits (Figure 8) revealed that the main phonon modes are as follows: E2(Low) at ≈88.97 cm^{-1}, E2(High) at ≈392.80 cm^{-1} and A1(TO) at ≈346.20 cm^{-1}, previously reported for hexagonal wurtzite [103–107]. The higher intensity of E2(Low) mode indicates that the vibrations of the heavy Zn sublattice are dominating in this structure, while the E2 of High frequency, attributed to the oxygen atoms, is at a significantly lower intensity. These facts may suggest that the ZnO structure of the deposits on the Mg-Ca0.3 presents defects because of the oxygen vacancies [108–110]. The shifts in the reported signals (Figure 8) have been influenced by the specifics of the Mg-Ca0.3 surface as substrate, as well as by ions impurities in the ZnO nanostructures, being a part of the used electrolytes for the electroless deposition [105,106,108].

3.1.8. X-ray Diffraction Patterns

In order to characterize the ZnO-NPs, a complementary analysis by XRD was carried out. The X-ray diffraction spectra of ZnO nanoparticles electroless deposited on Mg-Ca0.3 surface are presented in Appendix A to this manuscript (Figure A1). The peaks of X-ray diffraction are observed at 2θ values of 31.84°, 34.5°, 36.38°, 47.64°, 56.70° and 68.10°, which can be indexed for diffractions from the (100), (002), (101), (110), (103) and (112) planes, consistent with the hexagonal crystal structure of ZnO (wurtzite, JCPDS No. 361451).

3.2. Characterization of the Hybrid ZnO/Ag Electroless Deposits on Mg-Ca0.3

3.2.1. SEM-EDS Analysis

Figure 9 presents the SEM images (200× and 5000×) of the hybrid ZnO/Ag electroless deposits on the Mg-Ca0.3 surface. The EDS analysis suggested that more Ag was electroless nucleated on the ZnO/Mg-Ca0.3 substrate (Figure 9a–c), which surface was less covered by clusters of ZnO electroless, previously collected from the ZnO solution (Table 2).

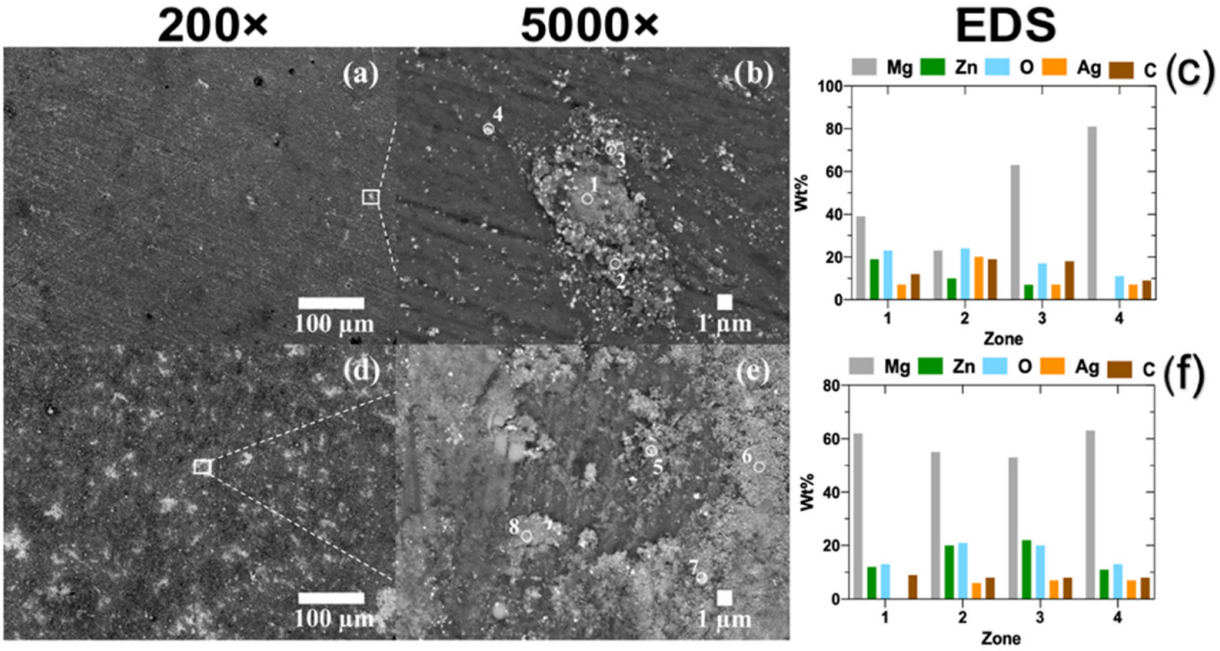

Figure 9. SEM images (200× and 5000×) and EDS analysis of electroless ZnO/Ag hybrid deposits achieved on ZnO/Mg-Ca0.3 surfaces obtained from aqueous solutions (10^{-3} M, at 21 °C): (**a–c**) ZnO/$AgNO_3$ and (**d–f**) $Zn(NO_3)_2$ /$AgNO_3$.

3.2.2. XPS Analysis

The surface analysis was performed to correlate with the EDS analyzes by zones (Figure 9c,f). The high-resolution XPS spectra were for ZnO/Ag hybrid electroless deposits on the Mg-Ca0.3 surface (Figure 10). In a similar way to ZnO nano-coating (Figure 3),

the high-resolution binding energy spectra identified the presence of $Mg(OH)_2$ (at ≈49.98 eV) [65–68], MgO (at ≈50.54 eV) [66,68,71,72,81], $MgCO_3$ (at ≈51.32 eV) [66,67,73], ZnO (at ≈1045.30 eV) [66,67,73–75,78–80] and $ZnCO_3$ (at ≈1022.40 eV) [78–80].

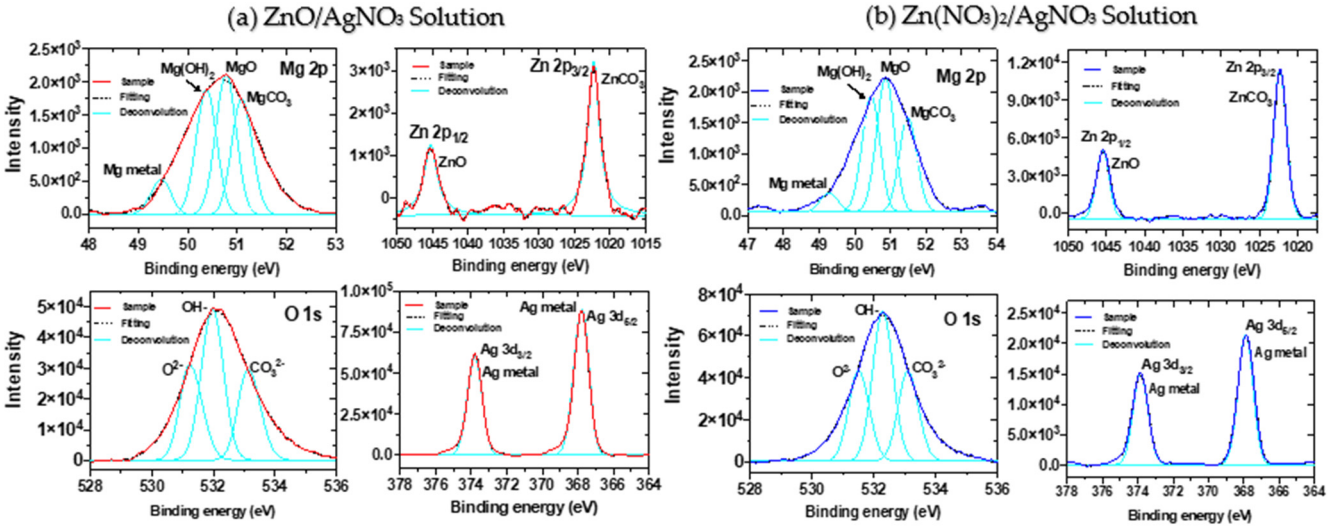

Figure 10. XPS spectra of ZnO/Ag hybrid deposits on Mg-Ca0.3 surface, electroless achieved from aqueous solutions (10^{-3} M, at 21 °C): (**a**) $ZnO/AgNO_3$ and (**b**) $Zn(NO_3)_2/AgNO_3$ solutions.

Furthermore, the spectrum of Ag displayed two characteristic peaks at ≈367.77 eV and ≈373.75 eV [66–69,71–77], and based on their intensities, it indicates that the higher concentration of electroless Ag deposit nucleated on the ZnO/Mg-Ca0.3 substrate. We propose that ZnO particles deposit first from the aqueous suspension of ZnO (Table 2). The deposition from ZnO suspension resulted in less coverage of the Mg-Ca0.3 substrate surface. This fact correlates well with the SEM-EDS analysis (Figure 9c).

3.2.3. EDS Mapping of the Elements

Similarly, the analysis of the EDS maps (200×) of the ZnO/Ag electroless deposits on the Mg-Ca0.3 surface (Figures 11 and 12) indicates that ≈2 times higher concentration of Ag was nucleated on the ZnO/Mg-Ca0.3 surface (Figure 11), which was less covered by clusters of electroless ZnO, previously obtained from ZnO solution without Ag (Table 1).

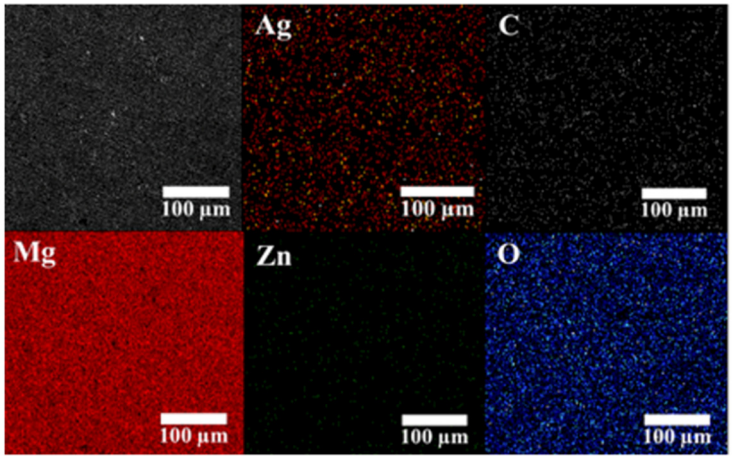

Elements	Weight %
Mg	61.42
O	12.40
Ag	16.49
Zn	6.47
C	3.22

Figure 11. EDS maps (200×) of the elements present in the hybrid ZnO/Ag deposits on Mg-Ca0.3 surfaces, electroless achieved from aqueous solutions (10^{-3} M, at 21 °C) $ZnO/AgNO_3$.

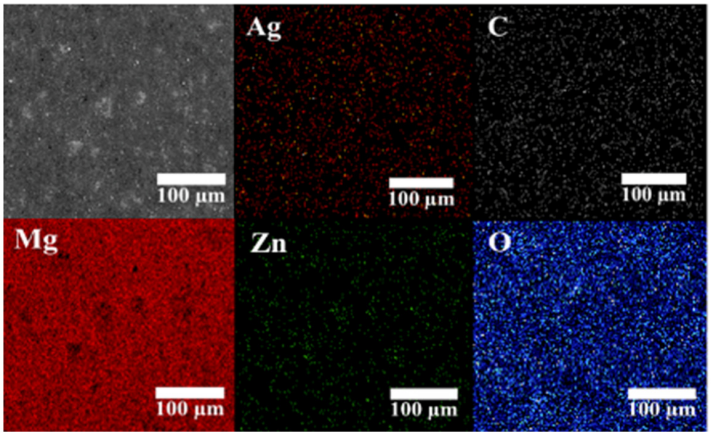

Elements	Weight %
Mg	51.45
O	16.04
Ag	8.50
Zn	18.61
C	5.42

Figure 12. EDS maps (200×) of the elements present in the hybrid ZnO/Ag deposits on Mg-Ca0.3 surfaces, electroless achieved from aqueous solutions (10^{-3} M, at 21 °C) $Zn(NO_3)_2$ /$AgNO_3$.

3.2.4. Ag Nano-Particle Size Distribution

The size distribution of Ag-NPs as part of ZnO/Ag hybrid deposits (Figure 13) indicates that Ag-NPs tend to nucleate and grow as islands in the substrate. Being a member of the wurtzite structural family, the ZnO surface exhibits a normal, non-central dipole moment in symmetry. These unique characteristics of ZnO, as well as the negative electrochemical potential of the Mg-Ca0.3 substrate during the electroless deposition (−1.17 V vs. SCE), may facilitate the attraction of positively charged Ag^+ ions and their deposition without electricity. The predominant sizes of Ag-NPs are ≈120 ± 3 nm (Figure 13a) and ≈94 ± 3 nm (Figure 13b). On the other hand, there is ≈2 times higher frequency of Ag-NPs nucleated on the ZnO deposits (Figure 13a) obtained from the ZnO aqueous suspension free of Ag (Table 2).

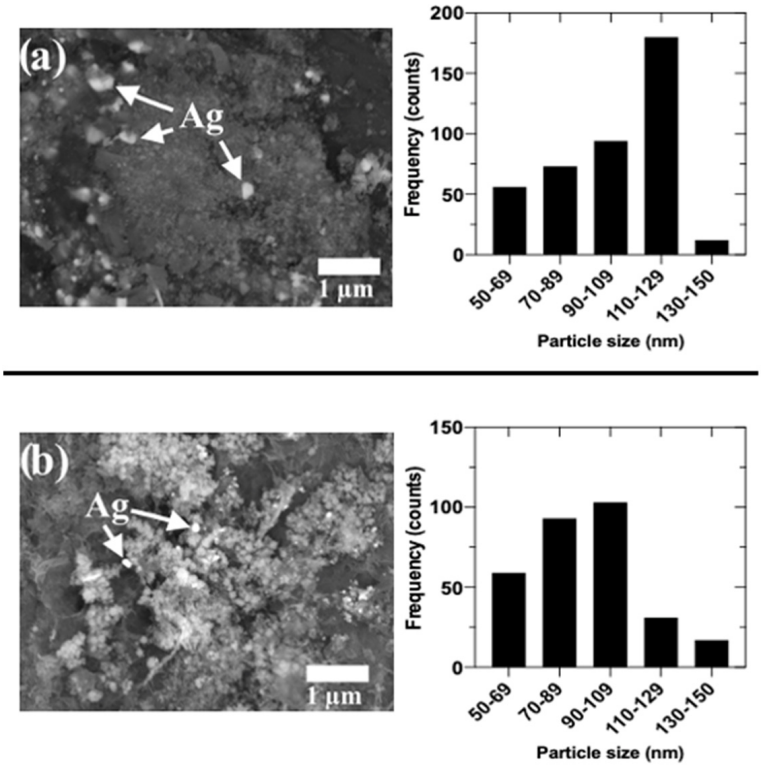

Figure 13. SEM images (20,000×) and particle size distribution of Ag as a part of the hybrid ZnO/Ag deposits on Mg-Ca0.3 surfaces, electroless achieved from aqueous solution (10^{-3} M, at 21 °C): (**a**) ZnO/$AgNO_3$ and (**b**) $Zn(NO_3)_2$/$AgNO_3$ solutions.

The measured open circuit potential (OCP) during the electroless deposition of ZnO on Mg-Ca0.3 was ≈−1.63 V (vs. SCE) and ≈−1.17 V (vs. SCE) on ZnO/Mg-Ca0.3 surface when the Ag-NPs were deposited; this 0.5 V difference is due to the free energy spent in the deposition of Ag^+ ions. We propose that there is a synergistic effect between the highly negative potential of the alloy (mostly of Mg) and the surface charges of ZnO/Mg-Ca0.3 that facilitate the deposition of Ag^+ ions.

3.2.5. UV-Visible Spectroscopy Analysis

Figure 14 shows the UV-Visible absorption spectra of the hybrid ZnO/Ag deposits on Mg-Ca0.3 alloy. The maximum peak at ≈380 nm is related to the optical behavior of ZnO-nanoparticles (NPs) [84–86,90], and the valley at ≈320 nm is attributed to the decrease in the imaginary part (k) of the refractive index of Ag-NPs [91].

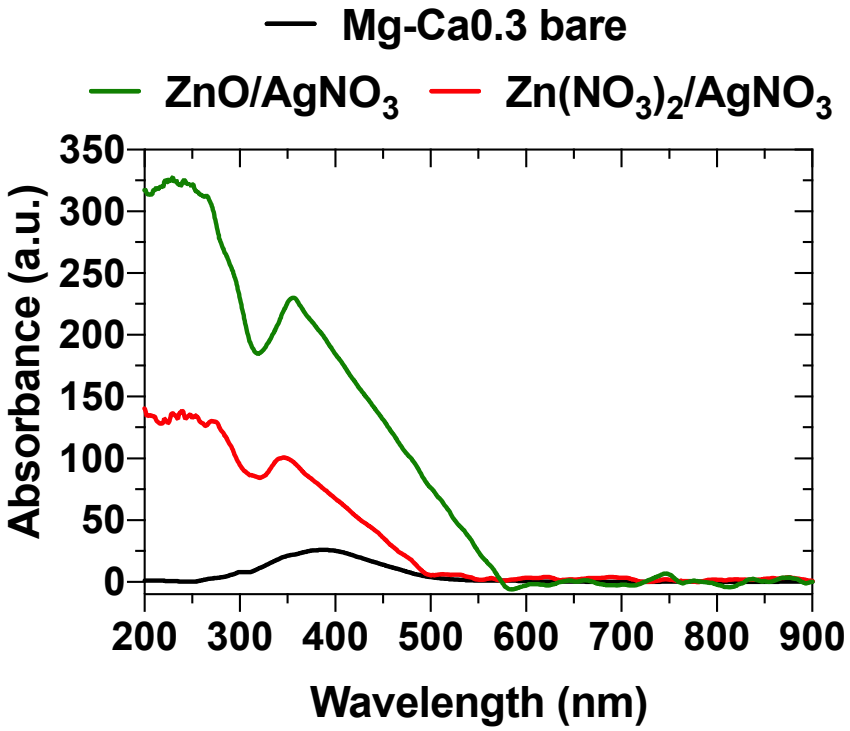

Figure 14. UV-Vis spectra of electroless hybrid ZnO/Ag-NPs deposits on Mg-Ca0.3 surfaces, electroless achieved from aqueous suspensions (10^{-3} M, at 21 °C): $ZnO/AgNO_3$ and $Zn(NO_3)_2/AgNO_3$ solutions.

The noise in this area of the spectrum is attributed to the low concentration of Ag-NPs added to the high optical absorbance associated with ZnO [92].

3.2.6. FTIR Analysis

The FTIR spectra (Specular Apertured Grazing Angle) of the hybrid electroless ZnO/Ag nano-particles deposits on Mg-Ca0.3 surfaces (Figure 15) revealed the characteristic peaks for the vibration of the Mg-O bond [82–85], hydroxyl group in $Mg(OH)_2$ [85,86] and carbonate group in $ZnCO_3$ [87,88], $MgCO_3$ [87,89] and Zn-O bond [90–95], all similar to those peaks corresponding to ZnO deposit (Figure 6b,c).

The presence of Ag-NPs in the deposits did not lead to significant changes or additional peaks in FTIR spectra (Figure 6b,c and Figure 15a,b), suggesting that chemical bonds between Ag, Mg and ZnO were not formed on most of the surface deposits [92].

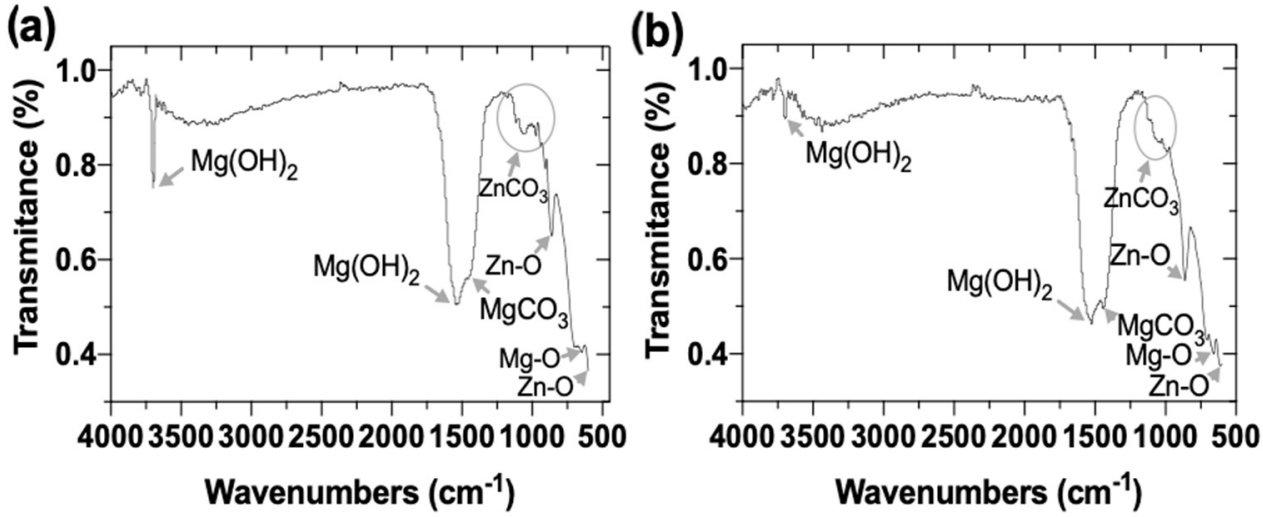

Figure 15. FTIR spectra of the hybrid ZnO/Ag-NPs deposits on Mg-Ca0.3 surfaces, electroless achieved from aqueous suspensions (10^{-3} M, at 21 °C): (**a**) ZnO/$AgNO_3$ and (**b**) $Zn(NO_3)_2$/AgNO.

3.2.7. Raman Spectroscopy Analysis

Figure 16 presents the Raman scattering spectra of the hybrid ZnO/Ag deposits. The peak of Ag detected at 230.94 cm^{-1} may associate with the Ag-O bond, according to the literature [111–114].

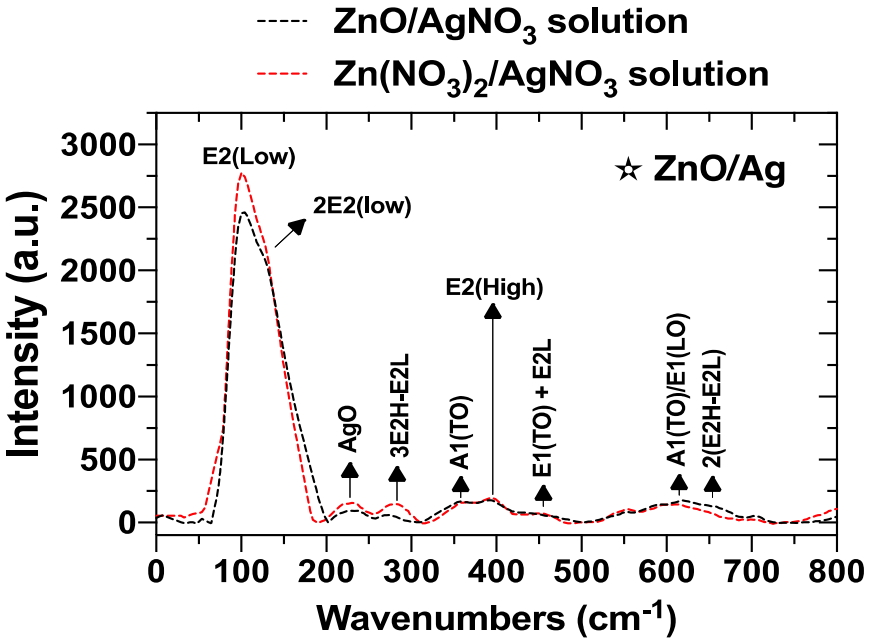

Figure 16. Raman spectra of hybrid ZnO/Ag-NPs deposits on the Mg-Ca0.3 surfaces, electroless achieved from (10^{-3} M, at 21 °C): ZnO/$AgNO_3$ and $Zn(NO_3)_2$/$AgNO_3$ suspensions.

When comparing the ZnO/Ag-NPs Raman spectra (Figure 16) with those of ZnO-NPs electroless deposits (Figure 6), noted that the intensity of the E2(Low) phonon mode of the Zn^{2+} ions has increased (Figure 16), consistent with the nucleation (deposition) process the Ag^{+} ions interacting with the negatively charged O^{2-} atoms, thus diminishing their polar moment. On the other hand, the main phonon modes of ZnO are as follows: E2(Low) at ≈100.6 cm^{-1}, E2(High) at ≈397.17 cm^{-1} and A1(TO) at ≈360.71 cm^{-1}. The shifts towards higher wave numbers may be attributed to the influence of the changed surface structure after the deposition of Ag-NPs from the $AgNO_3$ electrolyte.

3.2.8. X-ray Diffraction Patterns

To collaborate with the Ag-Nps characterization, an XRD analysis was carried out. The peaks of X-ray diffraction of Ag nanoparticles (Figure A2, Appendix A), electroless deposited on ZnO/Mg-Ca0.3, are observed at 2θ values of 38.18°, 44.25°, 64.72° and 77.46°, indexed for diffractions from the (111), (200), (220) and (311) planes, corresponding to the presence of Ag crystals of FCC cell structure (JCPDS No.04-0783). In our previous work, the Ag nanoparticles electroless deposited on Mg-Ca0.3 presented similar XRD spectra [45].

4. Conclusions

The hybrid of ZnO/Ag structures in the nanometer size, ca. 200 nm, were electroless deposited on Mg-Ca0.3 alloy surface, known as biodegradable and biocompatible material in physiological media. The ZnO NPs were achieved from 10^{-3} M aqueous solutions of ZnO (suspension) and $Zn(NO_3)_2$ on Mg-Ca0.3 substrate and later baked at 200 °C for 48 h. On the baked ZnO/Mg-Ca0.3 surface, Ag-NPs were electroless deposited from 10^{-3} M aqueous solution of $AgNO_3$; the hybrid ZnO/Ag deposits also were baked.

The electroless deposits were characterized by SEM-EDS, FTIR and XRD, as well as by UV-Visible and Raman spectroscopy, as sensitive diagnostic tools for nanocrystal structure.

The average size of solitary ZnO-NPs was estimated in the order of ≈85 nm, and once nucleated, the NPs tend to agglomerate; their coverage surface area is ≈2 times higher for the deposits obtained from $Zn(NO_3)_2$ solution.

XRD spectra of Ag-NPs indicated the presence of planes arranged with the FCC hexagonal structure.

Likewise, the Ag-NPs of electroless deposits, of an estimated size of ≈100 nm, nucleated in the vicinity of ZnO-NPs. The UV-Visible spectroscopy analysis identified the peak at ≈320 nm associated with the decrease in the imaginary part (k) of the refractive index of Ag-NPs, all consistent with the expectation that the Ag deposits correspond to metallic Ag in the nanoscale.

We propose that the Ag^+ ions were attracted by the negatively charged O^{2-} atoms of the Zn-O dipole, presenting the wurtzite structure, as suggested by Raman spectroscopy analysis. Thus, it may suggest that there is a synergistic effect between the highly negative potential of the alloy (mostly of Mg) and the surface charges of ZnO/Mg-Ca0.3 that facilitate the deposition of Ag^+ ions.

During the process of electroless deposition of the NPs of ZnO and Ag on the Mg-Ca0.3 surface, MgO, $Mg(OH)_2$ and $MgCO_3$ compounds were formed, according to XPS and FTIR.

Overall, the techniques are consistent with the deposition of a non-uniform layer that consists of crystalline nanoparticles. The deposition of ZnO is crystalline and of sufficient coverage so that it shows in the UV VIs. These nanoparticles of ZnO and Ag are in intimate contact based on the Raman results. The corrosion products on the surface suggest that the Mg is oxidized during the deposition of the Ag, which is consistent with a galvanic displacement reaction. The ZnO/Ag nanostructures are expected to provide antibacterial protection to the temporary structure.

The reported hybrid ZnO/Ag electroless deposits of NPs are of interest for temporary implant devices, providing antibacterial properties to Mg-Ca0.3 surface, used as biodegradable material.

Author Contributions: J.L.G.-M. performed the electroless deposition experiments and characterization of their surface. J.L.G.-M., V.L. and M.A.-A. discussed the results. J.L.G.-M. and V.L. wrote the manuscript. V.L. supervised the project. All correspondence should be directed to V.L. All authors have read and agreed to the published version of the manuscript.

Funding: FOMIX-Yucatán 2008-108160, CONACYT LAB-2009-01-123913, 292692, 294643, 188345 and 204822 and Grant NSF CHE-2108462 covered part of the publication funds.

Institutional Review Board Statement: Not applicable.

Informed Consent Statement: Not applicable.

Data Availability Statement: Data presented in this study are available on request from the corresponding author. The data are not public due to privacy issues.

Acknowledgments: J. Luis González-Murguía acknowledges the Mexican National Council for Science and Technology (CONCAYT) for the scholarship granted to him for his Ph.D. study. The authors gratefully thank the National Laboratory of Nano- and Biomaterials (LANNBIO-CINVESTAV) for allowing the use of DRX, SEM-EDS and XPS facilities, and to José Antonio Azamar-Barrios, Daniel Aguilar, Victor Rejón, José Bante and William Cauich for their support in data aquisition.

Conflicts of Interest: The authors declare no conflict of interest.

Appendix A

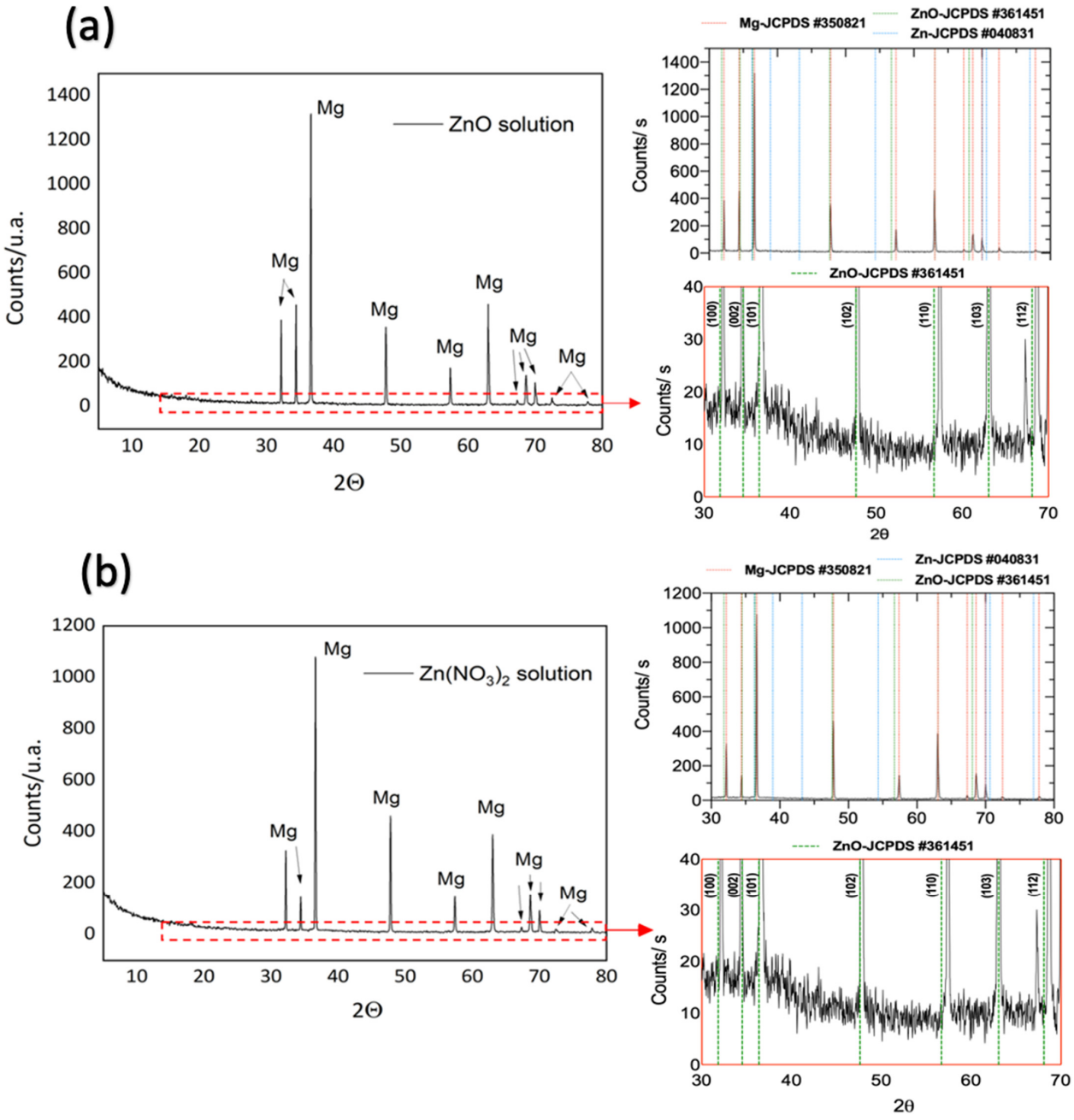

Figure A1. XRD spectra of ZnO-NPs electroless deposits on Mg-Ca0.3 surface achieved from 10^{-3} M solutions of ZnO (**a**) and $Zn(NO_3)_2$ (**b**).

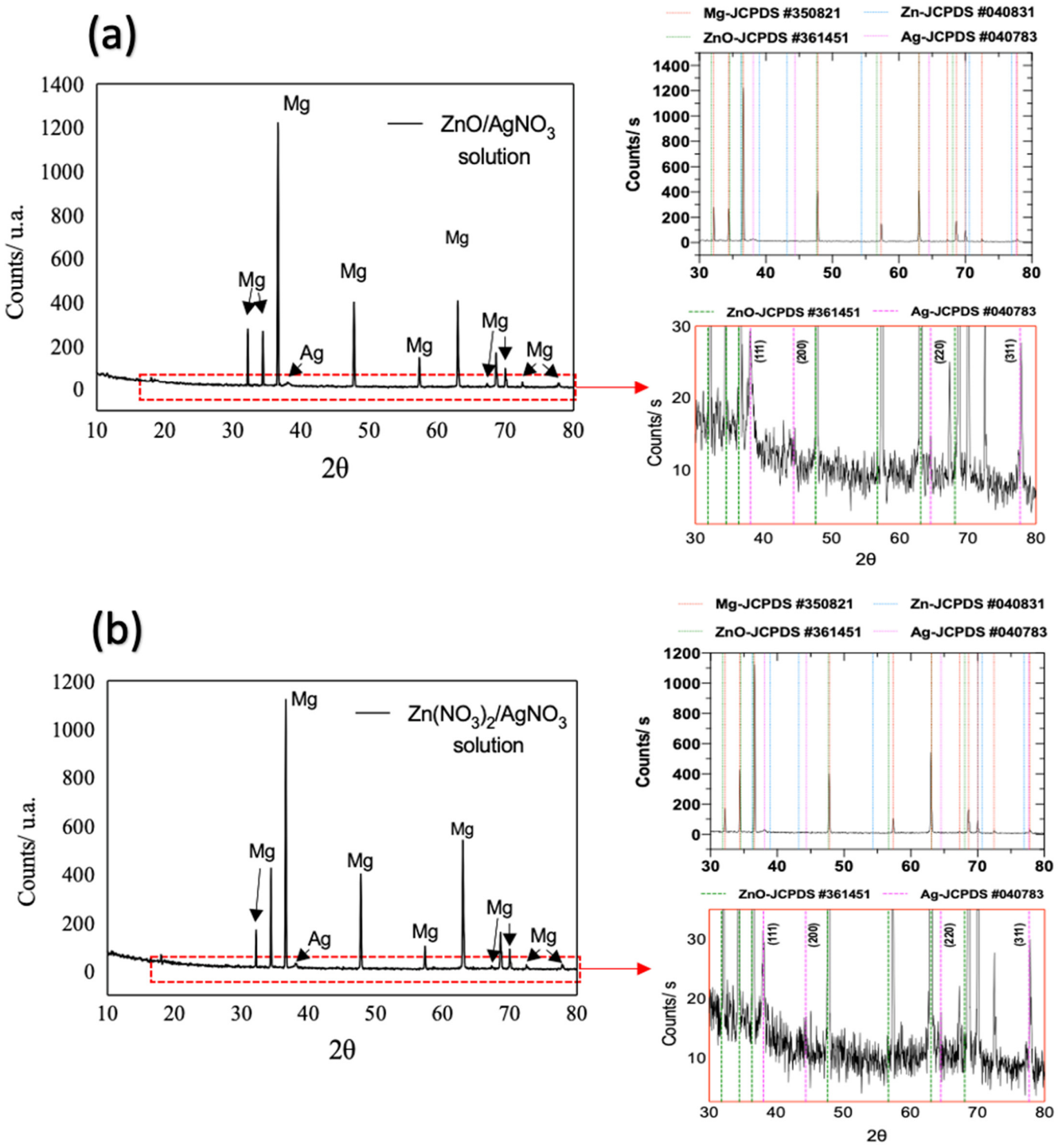

Figure A2. XRD spectra of Hybrid ZnO/Ag electroless deposits on Mg-Ca0.3 surface achieved from 10^{-3} M solutions of $ZnO/AgNO_3$ (**a**) and $Zn(NO_3)_2/AgNO_3$ (**b**).

References

1. Williams, D. New interest in magnesium. *Med. Device Technol.* **2006**, *17*, 9–10. Available online: https://scholar.google.com/scholar_lookup?title=New%20interests%20in%20magnesium&publication_year=2006&author=D.%20Williams (accessed on 15 June 2022). [PubMed]
2. Song, G.-L. Corrosion electrochemistry of magnesium (Mg) and its alloys. In *Corrosion of Magnesium Alloys*; Song, G.-L., Ed.; Woodhead Publishing: Cambridge, MA USA, 2011; pp. 3–65. ISBN 9781845697082.
3. Kirkland, N.T. Magnesium biomaterials: Past, present and future. *Corros. Eng. Sci. Technol.* **2012**, *47*, 322–328. [CrossRef]

4. Li, N.; Zheng, Y. Novel Magnesium Alloys Developed for Biomedical Application: A Review. *J. Mater. Sci. Technol.* **2013**, *29*, 489–502. [CrossRef]
5. Zheng, Y.; Gu, X.; Witte, F. Biodegradable metals. *Mater. Sci. Eng. R Rep.* **2014**, *77*, 1–34. [CrossRef]
6. Luthringer, B.; Feyerabend, F.; Willumeit, R. Magnesium-based implants: A mini-review. *Magnes. Res.* **2014**, *27*, 142–154. [CrossRef]
7. Tkacz, J.; Slouková, K.; Minda, J.; Drábiková, J.; Fintová, S.; Doležal, P.; Wasserbauer, J. Influence of the Composition of the Hank's Balanced Salt Solution on the Corrosion Behavior of AZ31 and AZ61 Magnesium Alloys. *Metals* **2017**, *7*, 465. [CrossRef]
8. Riaz, U.; Shabib, I.; Haider, W. The current trends of Mg alloys in biomedical applications—A review. *J. Biomed. Mater. Res. Part B Appl. Biomater.* **2018**, *107*, 1970–1996. [CrossRef]
9. Balakrishnan, P.; Sreekala, M.S.; Thomas, S. *Fundamental Biomaterials: Metals*, 1st ed.; Woodhead Publishing: Cambridge, MA, USA, 2018; pp. 23–24.
10. Chen, Y.-T.; Hung, F.-Y.; Syu, J.-C. Biodegradable Implantation Material: Mechanical Properties and Surface Corrosion Mechanism of Mg-1Ca-0.5Zr Alloy. *Metals* **2019**, *9*, 857. [CrossRef]
11. Tan, L.; Yu, X.; Wan, P.; Yang, K. Biodegradable Materials for Bone Repairs: A Review. *J. Mater. Sci. Technol.* **2013**, *29*, 503–513. [CrossRef]
12. La Pleshchitser, A. Biological Role of Magnesium. *Clin. Chem.* **1958**, *4*, 429–451. [CrossRef]
13. Hartwig, A. Role of magnesium in genomic stability. *Mutat. Res. Fundam. Mol. Mech. Mutagenesis* **2001**, *475*, 113–121. [CrossRef]
14. Revell, P.A.; Damien, E.; Zhang, X.; Evans, P.; Howlett, C.R. The Effect of Magnesium Ions on Bone Bonding to Hydroxyapatite Coating on Titanium Alloy Implants. *Key Eng. Mater.* **2003**, *254–256*, 447–450. [CrossRef]
15. Xue, D.; Yun, Y.; Tan, Z.; Dong, Z.; Schulz, M.J. In Vivo and In Vitro Degradation Behavior of Magnesium Alloys as Biomaterials. *J. Mater. Sci. Technol.* **2012**, *28*, 261–267. [CrossRef]
16. Razavi, M.; Fathi, M.; Savabi, O.; Tayebi, L.; Vashaee, D. Improvement of in vitro behavior of an Mg alloy using a nanostructured composite bioceramic coating. *J. Mater. Sci. Mater. Med.* **2018**, *29*, 159. [CrossRef] [PubMed]
17. Razavi, M.; Huang, Y. Assessment of magnesium-based biomaterials: From bench to clinic. *Biomater. Sci.* **2019**, *7*, 2241–2263. [CrossRef]
18. Witte, F. The history of biodegradable magnesium implants: A review. *Acta Biomater.* **2010**, *6*, 1680–1692. [CrossRef]
19. Chen, Q.; Thouas, G.A. Metallic implant biomaterials. *Mater. Sci. Eng. R Rep.* **2015**, *87*, 1–57. [CrossRef]
20. Wen, C.; Mabuchi, M.; Yamada, Y.; Shimojima, K.; Chino, Y.; Asahina, T. Processing of biocompatible porous Ti and Mg. *Scr. Mater.* **2001**, *45*, 1147–1153. [CrossRef]
21. Yamasaki, Y.; Yoshida, Y.; Okazaki, M.; Shimazu, A.; Uchida, T.; Kubo, T.; Akagawa, Y.; Hamada, Y.; Takahashi, J.; Matsuura, N. Synthesis of functionally graded $MgCO_3$ apatite accelerating osteoblast adhesion. *J. Biomed. Mater. Res.* **2002**, *62*, 99–105. [CrossRef] [PubMed]
22. Wolf, F.I.; Cittadini, A. Chemistry and biochemistry of magnesium. *Mol. Asp. Med.* **2003**, *24*, 3–9. [CrossRef]
23. Necula, B.S.; Fratila-Apachitei, L.E.; Berkani, A.; Apachitei, I.; Duszczyk, J. Enrichment of anodic MgO layers with Ag nanoparticles for biomedical applications. *J. Mater. Sci. Mater. Electron.* **2008**, *20*, 339–345. [CrossRef] [PubMed]
24. Sun, J.; Cai, S.; Li, Q.; Li, Z.; Xu, G. UV-irradiation induced biological activity and antibacterial activity of ZnO coated magnesium alloy. *Mater. Sci. Eng. C* **2020**, *114*, 110997. [CrossRef] [PubMed]
25. Carra, C.; Dell'Orto, E.; Morandi, V.; Riccardi, C. ZnO Nanostructured Thin Films via Supersonic Plasma Jet Deposition. *Coatings* **2020**, *10*, 788. [CrossRef]
26. Dulski, M.; Gawecki, R.; Sułowicz, S.; Cichomski, M.; Kazek-Kęsik, A.; Wala, M.; Leśniak-Ziółkowska, K.; Simka, W.; Mrozek-Wilczkiewicz, A.; Gawęda, M.; et al. Key Properties of a Bioactive Ag-SiO_2/TiO_2 Coating on NiTi Shape Memory Alloy as Necessary at the Development of a New Class of Biomedical Materials. *Int. J. Mol. Sci.* **2021**, *22*, 507. [CrossRef] [PubMed]
27. Góral, D.; Góral-Kowalczyk, M. Application of Metal Nanoparticles for Production of Self-Sterilizing Coatings. *Coatings* **2022**, *12*, 480. [CrossRef]
28. Nistor, C.L.; Mihaescu, C.I.; Bala, D.; Gifu, I.C.; Ninciuleanu, C.M.; Burlacu, S.G.; Petcu, C.; Vladu, M.-G.; Ghebaur, A.; Stroea, L.; et al. Novel Hydrophobic Nanostructured Antibacterial Coatings for Metallic Surface Protection. *Coatings* **2022**, *12*, 253. [CrossRef]
29. Kim, J.S.; Kuk, E.; Yu, K.N.; Kim, J.-H.; Park, S.J.; Lee, H.J.; Kim, S.H.; Park, Y.K.; Park, Y.H.; Hwang, C.-Y.; et al. Antimicrobial effects of silver nanoparticles. *Nanomed. Nanotechnol. Boil. Med.* **2007**, *3*, 95–101. [CrossRef]
30. Sondi, I.; Salopek-Sondi, B. Silver nanoparticles as antimicrobial agent: A case study on *E. coli* as a model for Gram-negative bacteria. *J. Colloid Interface Sci.* **2004**, *275*, 177–182. [CrossRef] [PubMed]
31. Alt, V.; Bechert, T.; Steinrücke, P.; Wagener, M.; Seidel, P.; Dingeldein, E.; Domann, E.; Schnettler, R. An in Vitro Assessment of the Antibacterial Properties and Cytotoxicity of Nanoparticulate Silver Bone Cement. *Biomaterials* **2004**, *25*, 4383–4391. [CrossRef]
32. Ohira, T.; Yamamoto, O. Correlation between antibacterial activity and crystallite size on ceramics. *Chem. Eng. Sci.* **2011**, *68*, 355–361. [CrossRef]
33. Jiang, Y.; Zhang, L.; Wen, D.; Ding, Y. Role of physical and chemical interactions in the antibacterial behavior of ZnO nanoparticles against E. coli. *Mater. Sci. Eng. C* **2016**, *69*, 1361–1366. [CrossRef]
34. Jiang, J.; Pi, J.; Cai, J. The Advancing of Zinc Oxide Nanoparticles for Biomedical Applications. *Bioinorg. Chem. Appl.* **2018**, *2018*, 1062562. [CrossRef] [PubMed]
35. Thirumoorthy, G.S.; Balasubramaniam, O.; Kumaresan, P.; Muthusamy, P.; Subramani, K. Tetraselmis indica Mediated Green Synthesis of Zinc Oxide (ZnO) Nanoparticles and Evaluating Its Antibacterial, Antioxidant, and Hemolytic Activity. *BioNanoScience* **2021**, *11*, 172–181. [CrossRef]

36. Coman, A.N.; Mare, A.; Tanase, C.; Bud, E.; Rusu, A. Silver-Deposited Nanoparticles on the Titanium Nanotubes Surface as a Promising Antibacterial Material into Implants. *Metals* **2021**, *11*, 92. [CrossRef]
37. Qing, Y.; Cheng, L.; Li, R.; Liu, G.; Zhang, Y.; Tang, X.; Wang, J.; Liu, H.; Qin, Y. Potential antibacterial mechanism of silver nanoparticles and the optimization of orthopedic implants by advanced modification technologies. *Int. J. Nanomed.* **2018**, *13*, 3311–3327. [CrossRef] [PubMed]
38. Burdușel, A.-C.; Gherasim, O.; Grumezescu, A.M.; Mogoantă, L.; Ficai, A.; Andronescu, E. Biomedical Applications of Silver Nanoparticles: An Up-to-Date Overview. *Nanomaterials* **2018**, *8*, 681. [CrossRef] [PubMed]
39. Cuadra, J.G.; Scalschi, L.; Vicedo, B.; Guc, M.; Izquierdo-Roca, V.; Porcar, S.; Fraga, D.; Carda, J.B. ZnO/Ag Nanocomposites with Enhanced Antimicrobial Activity. *Appl. Sci.* **2022**, *12*, 5023. [CrossRef]
40. Zreiqat, H.; Howlett, C.R.; Zannettino, A.; Evans, P.; Schulze-Tanzil, G.; Knabe, C.; Shakibaei, M. Mechanisms of magnesium-stimulated adhesion of osteoblastic cells to commonly used orthopaedic implants. *J. Biomed. Mater. Res.* **2002**, *62*, 175–184. [CrossRef]
41. Reyes-Vidal, Y.; Suarez-Rojas, R.; Ruiz, C.; Torres, J.; Ţălu, Ş.; Méndez, A.; Trejo, G. Electrodeposition, characterization, and antibacterial activity of zinc/silver particle composite coatings. *Appl. Surf. Sci.* **2015**, *342*, 34–41. [CrossRef]
42. Bakhsheshi-Rad, H.R.; Hamzah, E.; Ismail, A.F.; Aziz, M.; Kasiri-Asgarani, M.; Ghayour, H.; Razzaghi, M.; Hadisi, Z. In vitro corrosion behavior, bioactivity, and antibacterial performance of the silver-doped zinc oxide coating on magnesium alloy. *Mater. Corros.* **2017**, *68*, 1228–1236. [CrossRef]
43. Bakhsheshi-Rad, H.; Hamzah, E.; Ismail, A.F.; Aziz, M.; Kasiri-Asgarani, M.; Akbari, E.; Jabbarzare, S.; Najafinezhad, A.; Hadisi, Z. Synthesis of a novel nanostructured zinc oxide/baghdadite coating on Mg alloy for biomedical application: In-vitro degradation behavior and antibacterial activities. *Ceram. Int.* **2017**, *43*, 14842–14850. [CrossRef]
44. Coelho, P.G.; Jimbo, R. Osseointegration of metallic devices: Current trends based on implant hardware design. *Arch. Biochem. Biophys.* **2014**, *561*, 99–108. [CrossRef]
45. González-Murguía, J.L.; Veleva, L.; Rodríguez-Gattorno, G.; Figueroa-Torres, M.Z.; Feliu, S. Mg-Ca0.3 Electrochemical Activity Exposed to Hank's Physiological Solution and Properties of Ag-Nano-Particles Deposits. *Metals* **2021**, *11*, 1357. [CrossRef]
46. Barker, B. Electroless deposition of metals. *Surf. Technol.* **1981**, *12*, 77–88. [CrossRef]
47. Koura, N.; Kubota, A. Electroless plating of silver. *J. Met. Finish. Soc. Jpn.* **1985**, *36*, 182–190. [CrossRef]
48. Kerr, C.; Barker, D.; Walsh, F. Electroless Deposition of Metals. *Trans. IMF* **2001**, *79*, 41–46. [CrossRef]
49. Staňo, M.; Fruchart, O. Magnetic Nanowires and Nanotubes. *Handb. Magn. Mater.* **2018**, *27*, 155–267. [CrossRef]
50. Lahiri, A.; Pulletikurthi, G.; Endres, F. A Review on the Electroless Deposition of Functional Materials in Ionic Liquids for Batteries and Catalysis. *Front. Chem.* **2019**, *7*, 85. [CrossRef] [PubMed]
51. Jia, W.; Dang, S.; Liu, H.; Zhang, Z.; Yu, C.; Liu, X.; Xu, B. Evidence of the formation mechanism of ZnO in aqueous solution. *Mater. Lett.* **2012**, *82*, 99–101. [CrossRef]
52. Li, P.; Liu, H.; Lu, B.; Wei, Y. Formation Mechanism of 1D ZnO Nanowhiskers in Aqueous Solution. *J. Phys. Chem. C* **2010**, *114*, 21132–21137. [CrossRef]
53. Nagaya, S.; Nishikiori, H.; Mizusaki, H.; Wagata, H.; Teshima, K. Formation Process of Eosin Y-Adsorbing ZnO Particles by Electroless Deposition and Their Photoelectric Conversion Properties. *ACS Appl. Mater. Interfaces* **2015**, *7*, 11592–11598. [CrossRef] [PubMed]
54. Shinagawa, T.; Otomo, S.; Katayama, J.-I.; Izaki, M. Electroless deposition of transparent conducting and ⟨0001⟩-oriented ZnO films from aqueous solutions. *Electrochimica Acta* **2007**, *53*, 1170–1174. [CrossRef]
55. Donia, D.; Bauer, E.; Missori, M.; Roselli, L.; Cecchetti, D.; Tagliatesta, P.; Gontrani, L.; Carbone, M. Room Temperature Syntheses of ZnO and Their Structures. *Symmetry* **2021**, *13*, 733. [CrossRef]
56. Montazer, M.; Allahyarzadeh, V. Electroless Plating of Silver Nanoparticles/Nanolayer on Polyester Fabric Using Ag-NO_3/NaOH and Ammonia. *Ind. Eng. Chem. Res.* **2013**, *52*, 8436–8444. [CrossRef]
57. Brejna, P.R.; Griffiths, P.R. Electroless Deposition of Silver onto Silicon as a Method of Preparation of Reproducible Surface-Enhanced Raman Spectroscopy Substrates and Tip-Enhanced Raman Spectroscopy Tips. *Appl. Spectrosc.* **2010**, *64*, 493–499. [CrossRef]
58. Formanek, F.; Takeyasu, N.; Tanaka, T.; Chiyoda, K.; Ishikawa, A.; Kawata, S. Selective electroless plating to fabricate complex three-dimensional metallic micro/nanostructures. *Appl. Phys. Lett.* **2006**, *88*, 083110. [CrossRef]
59. Basuki, M.A.; Suryanto, H.; Larasati, A.; Puspitasari, P.; Mujiono. The effect of ZnO addition against crystallinity and water absorption capacity of biofoam based cassava starch reinforced bacterial cellulose. *AIP Conf. Proc.* **2019**, *2120*, 050016. [CrossRef]
60. Rezende, C.; Da Silva, J.; Mohallem, N. Influence of drying on the characteristics of zinc oxide nanoparticles. *Braz. J. Phys.* **2009**, *39*, 248–251. [CrossRef]
61. Kesim, Y.E.; Battal, E.; Okyay, A.K. Plasmonic materials based on ZnO films and their potential for developing broadband middle-infrared absorbers. *AIP Adv.* **2014**, *4*, 077106. [CrossRef]
62. Rad, H.R.B.; Idris, M.H.; Kadir, M.R.A.; Farahany, S. Microstructure analysis and corrosion behavior of biodegradable Mg-Ca implant alloys. *Mater. Des.* **2012**, *33*, 88–97. [CrossRef]
63. Liu, Y.; Liu, X.; Zhang, Z.; Farrell, N.; Chen, D.; Zheng, Y. Comparative, real-time in situ monitoring of galvanic corrosion in Mg-Mg2Ca and Mg-MgZn2 couples in Hank's solution. *Corros. Sci.* **2019**, *161*, 108185. [CrossRef]
64. Ding, Z.-Y.; Cui, L.-Y.; Chen, X.-B.; Zeng, R.-C.; Guan, S.-K.; Li, S.-Q.; Zhang, F.; Zou, Y.-H.; Liu, Q.-Y. In vitro corrosion of micro-arc oxidation coating on Mg-1Li-1Ca alloy—The influence of intermetallic compound Mg_2Ca. *J. Alloys Compd.* **2018**, *764*, 250–260. [CrossRef]

65. Khorasani, F.; Emamy, M.; Malekan, M.; Mirzadeh, H.; Pourbahari, B.; Krajnák, T.; Minárik, P. Enhancement of the microstructure and elevated temperature mechanical properties of as-cast Mg-Al2Ca-Mg2Ca in-situ composite by hot extrusion. *Mater. Charact.* **2018**, *147*, 155–164. [CrossRef]
66. Haycock, D.E.; Kasrai, M.; Nicholls, C.J.; Urch, D.S. The electronic structure of magnesium hydroxide (brucite) using X-ray emission, X-ray photoelectron, and auger spectroscopy. *J. Chem. Soc. Dalton Trans.* **1978**, *12*, 1791–1796. [CrossRef]
67. Moulder, J.F.; Stickle, W.E.; Sobol, P.E.; Bomben, K.D. *Handbook of X-ray Photoelectron Spectroscopy*; Chastian, J., Ed.; Perkin—Elmer-Corp: Lansing, MI, USA, 1992.
68. Naumkin, A.V.; Kraut-Vass, A.; Gaarenstroom, S.W.; Powell, C.J. *NIST X-ray Photoelectron Spectroscopy Database, Version 4.1*; National Institute of Standards and Technology: Gaithersburg, MD, USA, 2012. Available online: http://srdata.nist.gov/xps/ (accessed on 15 June 2022).
69. Saleh, H.; Weling, T.; Seidel, J.; Schmidtchen, M.; Kawalla, R.; Mertens, F.O.R.L.; Vogt, H.-P. An XPS Study of Native Oxide and Isothermal Oxidation Kinetics at 300 °C of AZ31 Twin Roll Cast Magnesium Alloy. *Oxid. Met.* **2013**, *81*, 529–548. [CrossRef]
70. Huang, C.-H.; Jan, Y.-L.; Lu, P.-T. Investigation of Approaches to Control the Compositions of Zn(Se,OH) Buffers Prepared by Chemical Bath Deposition Process for Cu(In,Ga)Se2 (CIGS) Solar Cells. *Crystals* **2018**, *8*, 343. [CrossRef]
71. Yao, H.; Li, Y.; Wee, A. An XPS investigation of the oxidation/corrosion of melt-spun Mg. *Appl. Surf. Sci.* **2000**, *158*, 112–119. [CrossRef]
72. Fournier, V.; Marcus, P.; Olefjord, I. Oxidation of magnesium. *Surf. Interface Anal.* **2002**, *34*, 494–497. [CrossRef]
73. Lindsay, R.; Thornton, G. Structure of Atomic and Molecular Adsorbates on Low-Miller-Index ZnO Surfaces Using X-ray Absorption Spectroscopy. *Top. Catal.* **2002**, *18*, 15–19. [CrossRef]
74. Rössler, N.; Kotsis, K.; Staemmler, V. Ab initio calculations for the Zn 2s and 2p core level binding energies in Zn oxo compounds and ZnO. *Phys. Chem. Chem. Phys.* **2006**, *8*, 697–706. [CrossRef] [PubMed]
75. Ballerini, G.; Ogle, K.; Barthés-Labrousse, M.-G. The acid–base properties of the surface of native zinc oxide layers: An XPS study of adsorption of 1,2-diaminoethane. *Appl. Surf. Sci.* **2007**, *253*, 6860–6867. [CrossRef]
76. Hoogewijs, R.; Fiermans, L.; Vennik, J. Electronic relaxation processes in the KLL′ auger spectra of the free magnesium atom, solid magnesium and MgO. *J. Electron Spectrosc. Relat. Phenom.* **1977**, *11*, 171–183. [CrossRef]
77. Corneille, J.S.; He, J.-W.; Goodman, D. XPS characterization of ultra-thin MgO films on a Mo(100) surface. *Surf. Sci.* **1994**, *306*, 269–278. [CrossRef]
78. Rößler, N.; Staemmler, V. Ab initio calculations for the 2s and 2p core level binding energies of atomic Zn, Zn metal, and Zn containing molecules. *Phys. Chem. Chem. Phys.* **2003**, *5*, 3580–3586. [CrossRef]
79. Feng, Q.; Wen, S. Formation of zinc sulfide species on smithsonite surfaces and its response to flotation performance. *J. Alloys Compd.* **2017**, *709*, 602–608. [CrossRef]
80. Dake, L.S.; Baer, D.R.; Zachara, J.M. Auger parameter measurements of zinc compounds relevant to zinc transport in the environment. *Surf. Interface Anal.* **1989**, *14*, 71–75. [CrossRef]
81. Zachara, J.; Kittrick, J.; Dake, L.; Harsh, J. Solubility and surface spectroscopy of zinc precipitates on calcite. *Geochim. et Cosmochim. Acta* **1989**, *53*, 9–19. [CrossRef]
82. Chowdhury, A.H.; Ghosh, S.; Islam, S.M. Flower-like AgNPs@m-MgO as an excellent catalyst for CO_2 fixation and acylation reactions under ambient conditions. *New J. Chem.* **2018**, *42*, 14194–14202. [CrossRef]
83. Farias, S.A.S.; Longo, E.; Gargano, R.; Martins, J.B.L. CO_2 adsorption on polar surfaces of ZnO. *J. Mol. Model.* **2012**, *19*, 2069–2078. [CrossRef]
84. Selvam, N.C.S.; Kumar, R.T.; Kennedy, L.J.; Vijaya, J.J. Comparative study of microwave and conventional methods for the preparation and optical properties of novel MgO-micro and nano-structures. *J. Alloys Compd.* **2011**, *509*, 9809–9815. [CrossRef]
85. Zahir, M.H.; Rahman, M.M.; Irshad, K. Shape-Stabilized Phase Change Materials for Solar Energy Storage: MgO and $Mg(OH)_2$ Mixed with Polyethylene Glycol. *Nanomaterials* **2019**, *9*, 1773. [CrossRef] [PubMed]
86. Ansari, A.; Ali, A.; Asif, M.; Shamsuzzaman, S. Microwave-assisted MgO NP catalyzed one-pot multicomponent synthesis of polysubstituted steroidal pyridines. *New J. Chem.* **2017**, *42*, 184–197. [CrossRef]
87. John, M. Low Temperature Synthesis of Nano Crystalline Zero-Valent Phases and (Doped) Metal Oxides as AxB3−xO4 (Ferrite), ABO2 (Delafossite), A2O and AO. A New Process to Treat Industrial Wastewaters? Ph.D. Thesis, Ludwig-Maximilians-Universität München, Munich, Germany, 2015. [CrossRef]
88. Sharma, V.; Basak, S.; Rishabh, K.; Umaria, H.; Ali, S.W. Synthesis of zinc carbonate nanoneedles, a potential flame retardant for cotton textiles. *Cellulose* **2018**, *25*, 6191–6205. [CrossRef]
89. Mancarella, F.; D'Elia, M.; Longo, G.M.; Longo, S.; Orofino, V. Kinetics of Thermal Decomposition of Particulate Samples of $MgCO_3$: Experiments and Models. *Chemistry* **2022**, *4*, 548–559. [CrossRef]
90. Maddahi, P.; Shahtahmasebi, N.; Kompany, A.; Mashreghi, M.; Safaee, S.; Roozban, F. Effect of doping on structural and optical properties of ZnO nanoparticles: Study of antibacterial properties. *Mater. Sci.* **2014**, *32*, 130–135. [CrossRef]
91. Zamiri, R.; Rebelo, A.; Zamiri, G.; Adnani, A.; Kuashal, A.; Belsley, M.S.; Ferreira, J.M.F. Far-infrared optical constants of ZnO and ZnO/Ag nanostructures. *RSC Adv.* **2014**, *4*, 20902–20908. [CrossRef]
92. Saoud, K.; Alsoubaihi, R.; Bensalah, N.; Bora, T.; Bertino, M.; Dutta, J. Synthesis of supported silver nano-spheres on zinc oxide nanorods for visible light photocatalytic applications. *Mater. Res. Bull.* **2015**, *63*, 134–140. [CrossRef]
93. Hoseinpour, V.; Souri, M.; Ghaemi, N.; Shakeri, A. Optimization of green synthesis of ZnO nanoparticles by *Dittrichia grave-olens* (L.) aqueous extract. *HBB* **2017**, *2*, 39–49. [CrossRef]

94. Nagaraju, G.; Udayabhanu; Shivaraj; Prashanth, S.; Shastri, M.; Yathish, K.; Anupama, C.; Rangappa, D. Electrochemical heavy metal detection, photocatalytic, photoluminescence, biodiesel production and antibacterial activities of Ag–ZnO nanomaterial. *Mater. Res. Bull.* **2017**, *94*, 54–63. [CrossRef]
95. Abdullah, E.A.; Anber, A.A.; Edan, F.F.; Fraih, A.J. Synthesis of ZnO Nanoparticles by Using an Atmospheric-Pressure Plasma Jet. *OALib* **2018**, *5*, e4755. [CrossRef]
96. Zak, A.K.; Razali, R.; Majid, W.H.B.A.; Darroudi, M. Synthesis and characterization of a narrow size distribution of zinc oxide nanoparticles. *Int. J. Nanomed.* **2011**, *6*, 1399–1403. [CrossRef]
97. Gurgur, E.; Oluyamo, S.S.; Adetuyi, A.O.; Omotunde, O.I.; Okoronkwo, A.E. Green synthesis of zinc oxide nanoparticles and zinc oxide–silver, zinc oxide–copper nanocomposites using Bridelia ferruginea as biotemplate. *SN Appl. Sci.* **2020**, *2*, 911. [CrossRef]
98. Spanhel, L.; Anderson, M.A. Semiconductor clusters in the sol-gel process: Quantized aggregation, gelation, and crystal growth in concentrated zinc oxide colloids. *J. Am. Chem. Soc.* **1991**, *113*, 2826–2833. [CrossRef]
99. Bahnemann, D.W.; Kormann, C.; Hoffmann, M.R. Preparation and characterization of quantum size zinc oxide: A detailed spectroscopic study. *J. Phys. Chem.* **1987**, *91*, 3789–3798. [CrossRef]
100. Monticone, S.; Tufeu, R.; Kanaev, A.V. Complex Nature of the UV and Visible Fluorescence of Colloidal ZnO Nanoparticles. *J. Phys. Chem. B* **1998**, *102*, 2854–2862. [CrossRef] [PubMed]
101. Rodríguez-Gattorno, G.; Santiago-Jacinto, P.; Rendon-Vázquez, L.; Németh, J.; Dékány, I.; Díaz, D. Novel Synthesis Pathway of ZnO Nanoparticles from the Spontaneous Hydrolysis of Zinc Carboxylate Salts. *J. Phys. Chem. B* **2003**, *107*, 12597–12604. [CrossRef]
102. Németh, J.; Rodríguez-Gattorno, G.; Diaz, D.; Vázquez-Olmos, A.R.; Dékány, I. Synthesis of ZnO Nanoparticles on a Clay Mineral Surface in Dimethyl Sulfoxide Medium. *Langmuir* **2004**, *20*, 2855–2860. [CrossRef] [PubMed]
103. Umar, A.; Karunagaran, B.; Suh, E.-K.; Hahn, Y.B. Structural and optical properties of single-crystalline ZnO nanorods grown on silicon by thermal evaporation. *Nanotechnology* **2006**, *17*, 4072–4077. [CrossRef]
104. Khan, A.; Kordesch, M.E. Synthesis of novel zinc oxide microphone-like microstructures. *Mater. Lett.* **2008**, *62*, 230–234. [CrossRef]
105. Aurangzeb, K. Raman Spectroscopic Study of The ZnO Nanostructures. *J. Pak Mater. Soc.* **2010**, *4*, 5–9. Available online: https://scholar.google.com/scholar_lookup?title=Raman%20spectroscopic%20study%20of%20the%20ZnO%20nanostructures&publication_year=2010&author=A.%20Khan (accessed on 15 June 2022).
106. Silambarasan, M.; Saravanan, S.; Soga, T. Raman and Photoluminescence Studies of Ag and Fe-doped ZnO Nanoparticles. *Int. J. Chemtech. Res.* **2015**, *7*, 1644–1650. Available online: https://scholar.google.com/scholar_lookup?title=Raman+and+photoluminescence+studies+of+Ag+and+Fe-doped+ZnO+nanoparticles&author=Silambarasan,+M.&author=Saravanan,+S.&author=Soga,+T.&publication_year=2015&journal=Int.+J.+Chem.+Technol.+Res.&volume=7&pages=1644%E2%80%931650 (accessed on 15 June 2022).
107. Xu, C.X.; Sun, X.; Zhang, X.H.; Ke, L.; Chua, S.J. Photoluminescent properties of copper-doped zinc oxide nanowires. *Nanotechnology* **2004**, *15*, 856–861. [CrossRef]
108. Huerta-Flores, A.M.; Luévano-Hipólito, E.; Torres-Martínez, L.M.; Torres-Sánchez, A. Photocatalytic H_2 production and CO_2 reduction on Cu, Ni-doped ZnO: Effect of metal doping and oxygen vacancies. *J. Mater. Sci. Mater. Electron.* **2019**, *30*, 18506–18518. [CrossRef]
109. Russo, V.; Ghidelli, M.; Gondoni, P.; Casari, C.S.; Bassi, A.L. Multi-wavelength Raman scattering of nanostructured Al-doped zinc oxide. *J. Appl. Phys.* **2014**, *115*, 073508. [CrossRef]
110. Fukushima, H.; Uchida, H.; Funakubo, H.; Katoda, T.; Nishida, K. Evaluation of oxygen vacancies in ZnO single crystals and powders by micro-Raman spectroscopy. *J. Ceram. Soc. Jpn.* **2017**, *125*, 445–448. [CrossRef]
111. Débarre, A.; Jaffiol, R.; Julien, C.; Tchénio, P.; Mostafavi, M. Raman scattering from single Ag aggregates in presence of EDTA. *Chem. Phys. Lett.* **2004**, *386*, 244–247. [CrossRef]
112. Van Der Horst, C.; Silwana, B.; Iwuoha, E.; Somerset, V.S. Synthesis and Characterization of Bismuth-Silver Nanoparticles for Electrochemical Sensor Applications. *Anal. Lett.* **2014**, *48*, 1311–1332. [CrossRef]
113. Lai, C.-H.; Wang, G.-A.; Ling, T.-K.; Wang, T.-J.; Chiu, P.-K.; Chau, Y.-F.C.; Huang, C.-C.; Chiang, H.-P. Near infrared surface-enhanced Raman scattering based on star-shaped gold/silver nanoparticles and hyperbolic metamaterial. *Sci. Rep.* **2017**, *7*, 5446. [CrossRef] [PubMed]
114. Joshi, N.; Jain, N.; Pathak, A.; Singh, J.; Prasad, R.; Upadhyaya, C.P. Biosynthesis of silver nanoparticles using Carissa carandas berries and its potential antibacterial activities. *J. Sol-Gel Sci. Technol.* **2018**, *86*, 682–689. [CrossRef]